STATISTICAL PROPERTIES OF RANDOM FRACTALS: GEOMETRY, GROWTH AND INTERFACE DYNAMICS

Joonas Asikainen

Laboratory of Physics
Helsinki University of Technology

Fysiikan laboratorio
Teknillinen korkeakoulu

DISSERTATION 118 (2002)

STATISTICAL PROPERTIES OF RANDOM FRACTALS: GEOMETRY, GROWTH AND INTERFACE DYNAMICS

Joonas Asikainen

Laboratory of Physics
Helsinki University of Technology
Espoo, Finland

Dissertation for the degree of Doctor of Science in Technology to be presented with due permission of the Department of Engineering Physics and Mathematics, Helsinki University of Technology for public examination and debate in Auditorium K at Helsinki University of Technology (Espoo, Finland) on the 23rd of November, 2002, at 12 o'clock noon.

Dissertations of Laboratory of Physics, Helsinki University of Technology
ISSN 1455-1802

Dissertation 118 (2002):
Joonas Asikainen: Statistical properties of random fractals: geometry, growth and interface dynamics
ISBN 951-22-6204-5 (print)
ISBN 951-22-6205-3 (electronic)

OTAMEDIA OY
ESPOO 2002

To Elias and Sofia.

Abstract

This thesis comprises analytic and numerical studies of static, geometrical properties of fractals and dynamical processes in them. First, we have numerically estimated the subset fractal dimensions D_S describing the scaling of some subsets S of the fractal cluster with the linear cluster size R in the q-state Potts models. These subsets include the total mass of the cluster, the hull, the external perimeter, the singly connected bonds and the gates to fjords. Numerical data reveals complex corrections-to-scaling behavior needed to take into account for correct extrapolation of the data to the asymptotic large size limit. Using renormalization group theory the corrections-to-scaling terms are analytically derived. The numerical data are in good agreement with exact values of the fractal dimensions and with the exactly predicted correction terms. Regarding the growth of fractal structures, we consider 2D continuum deposition models which generate fractal structures from the point of view of percolation theory. In the particular model studied here, there is an effective inter-particle rejection. Using previous results from related irreversible deposition models mean field predictions for the percolation thresholds of the model are derived in the limits of the parameter space defining the model. Numerical simulations of the model support the theoretical results. The networks exhibit non-trivial spatial correlations, which manifest themselves in a power-law behavior of the mass density fluctuation correlation function for small distances. Geometric properties of fractals play a crucial role in the dynamics and kinetic roughening of driven fronts in fractals. Here we show that for the isotropic invasion percolation model, an algebraically decaying distribution for the nearest neighbor slope distribution of single-valued fronts follows from scaling arguments derived using the properties of percolation clusters. From the distribution, the form of which is also valid for anisotropic cases such as the diffusion limited aggregation model, the exponents governing the scaling of various spatio-temporal correlation functions are derived. The results indicate that the fractal growth models exhibit intrinsic anomalous scaling and multiscaling. Numerical simulations show excellent agreement with the predictions.

Preface

This thesis has been prepared in Laboratory of Physics at Helsinki University of Technology during the years 1998 - 2002.

I wish to thank my advisors Prof. Tapio Ala-Nissilä from Helsinki University of Technology and Prof. Amnon Aharony from Tel Aviv University, Israel. Tapio offered me the opportunity to conduct my graduate studies and research in his group. I wish to thank him for this and for his guidance especially with the topics concerning surface physics. I wish to thank Amnon for the chance to work on an international project and for teaching me a lot about fractals and scaling.

I also wish to thank all the coauthors of the publications included in this thesis, especially Martin Dubé, Jarkko Heinonen and Sami Majaniemi. Furthermore, I wish to thank the pre-examiners Dr. Mario Castro and Doc. Juha Merikoski for careful reading of the manuscript and useful comments.

Thanks belong to the members of the Statistical Physics and Materials Science group at Laboratory of Physics at Helsinki University of Technology for pleasant working atmosphere. In particular, I want to thank Marko Rusanen for helpful discussions and many practical hints.

The administrative personnel of the Laboratory also deserve my gratitude. I wish to thank the Väisälä foundation and the National Graduate School in Materials Physics for financial support.

The greatest support during these years has, however, come from my wife Annukka. I want to thank her for encouragement, and especially for loving me.

Espoo, October 2002

Joonas Asikainen

Contents

List of publications

This thesis consists of an overview and the following publications:

I N. Provatas, M. Haataja, J. Asikainen, S. Majaniemi, M. Alava, and T. Ala-Nissila, "Fiber deposition models in two and three spatial dimensions", invited review in Colloids and Surfaces A **165**, 209 (2000).

II J. Asikainen and T. Ala-Nissila, "Percolation and spatial correlations in a two-dimensional continuum deposition model", Phys. Rev. E **61**, 5002 (2000).

III A. Aharony and J. Asikainen, "Fractal dimensions and corrections to scaling for critical Potts clusters", Fractals (2001) (in press).

IV J. Asikainen, S. Majaniemi, M. Dubé and T. Ala-Nissila, "Interface Dynamics and Kinetic Roughening in Fractals", Phys. Rev. E **65**, 052104 (2002).

V J. Asikainen, S. Majaniemi, M. Dubé, J. Heinonen and T. Ala-Nissila, "Dynamics, Scaling and Kinetic Roughening of Single Valued Fronts Propagating in Fractal Media", accepted for publication in Eur. Phys. J. B.

VI J. Asikainen, J. Heinonen and T. Ala-Nissila, "Exact and efficient discrete random walk algorithm for time-dependent environments", accepted for publication in Phys. Rev. E.

The author has played an active role in all stages of the research work reported in this thesis. He has been involved in deriving the analytical results reported in the publications. He has designed and implemented all the simulation programs himself, and performed all the numerical calculations and data analysis except for a part of the calculations done for Publication I. The

author has written publications II, IV, V and VI, and contributed actively to the writing of the other papers. In addition, this thesis includes numerical data for the geometry of Potts clusters from an unpublished manuscript [1].

Chapter 1

Introduction

Lattice models of magnetic materials [2, 3] and a variety of fractal models [4, 5, 6] have played a fundamental role in the development of statistical physics [7, 8, 9]. Such models are based on simplification of the phenomena found in real systems by e.g. reducing the degrees of freedom and simplifying the interactions. Most of the models share the goal of describing phenomena found in nature [7, 10, 11] and various fractal models have been used in cancer research [12, 13] and biological pattern formation [14].

Methods for studying fractals range from experimental measurements to computer simulations and highly involved theoretical approaches [8, 15]. Analytical methods include renormalization group calculations [16, 17], mapping to other exactly solvable models [18], considerations of path crossing probabilities [19] and conformal field theory combined with quantum gravity [20]. Numerical methods are of great importance in the study of such models [8, 21, 22, 23]. In addition, a lot of experimental work has been devoted to study these models [24, 25, 26, 27, 28, 29].

Many simple models are known to generate fractal structures. A fractal is, loosely speaking, an object that looks the same at every length scale. Fractals arising in nature, however, have some cutoffs in length scales, beyond which this *self-similarity* does not hold. More quantitatively, a fractal is defined through the *fractal dimension* $D < d$ (d is the spatial dimension), which describes the scaling of the mass M of the fractal with its size R [15]: $M(R) \propto R^D$.

A large variety of fractals, both fractals in nature and fractal models, have been target of extensive studies during the past decades [8, 9, 15, 30]. Examples of natural fractal structures include snow flakes, the coast line of Norway,

etc. [15] . Fractal models include deterministic fractal models such as the Sierpinski carpet and Sierpinski gasket [8, 15] and random fractals such as the percolation cluster [7, 8].

If the fractal objects are invariant under isotropic transformations they are called *self-similar* [9]. In contrast, if the object is invariant under anisotropic transformation it is called *self-affine* [9]. An example of a self-similar fractal is the percolation cluster [8]. Many fractal growth models such as the ballistic deposition model produce self-affine structures [9]. For classification of fractals, consideration of the bare fractal dimension D is not sufficient. Mandelbrot [15] introduced the concept of *fractal geometry* to study the geometrical properties of fractals and to differentiate between various fractals. Fractal geometry deals with the scaling of various cluster subsets with the cluster size.

Irreversible deposition models constitute an important class of models producing fractal structures. A variety of models have been developed to study deposition phenomena found in nature, where various transport mechanisms bring particles to a surface [31, 32, 33, 34, 35, 36, 37]. These types of models have been used to model many physical, chemical and biological processes.

A particularly interesting example involving particle deposition can occur in the case of colloidal suspensions. For some such systems, the inter-particle repulsion is strong enough to prevent multilayer growth [32]. However, the existence of dispersion forces can change this repulsion so that even particle aggregation and subsequent precipitation out of the suspension may occur [38, 39]. For larger particles or clusters of particles, gravity must also be taken into account and can in part help to overcome inter-particle repulsion. A full microscopic treatment of many deposition processes such as sedimentation is a formidable task [40].

In addition to their practical applications, 2D random deposition models have been the topic of intense study in the context of continuum percolation theory [33, 41, 42, 43, 44, 36, 37, 45, 46]. The quantity of central importance in these studies is the percolation threshold or critical particle density, which for permeable objects can be related to the *excluded volume* of the particles [47].

The so-called "flocculation model" (FM) [36] was developed to capture some of the features characterizing formation of laboratory paper. In the process, cellulose fibers filtrate from the fiber suspension onto a mesh. Fibers are known to form flocks [33], and this tendency is modeled via an effective attractive interaction described by a parameter p. By tuning the sticking

probability p one can interpolate between uniformly random fiber network ($p \to 1$) and the case where only one cluster grows from a seed fiber ($p \to 0$). In the intermediate values of p, interaction causes the network to form of fiber flocks, resulting in non-trivial power-law form of the two-point mass density fluctuation correlation function. The results can be contrasted with those obtained for mass density correlations in real paper sheets [48].

Fractal concepts are important in understanding the transport processes where the background itself is fractal [9]. Flow, dispersion and displacement processes in porous media arise in many diverse fields of science and engineering, ranging from agricultural, biomedical, construction, ceramic, chemical, and petroleum engineering to food and soil sciences and powder metallurgy [11]. Various applications include ground water hydrology, drainage and irrigation engineering, and sanitary engineering [10]. As an example of a problem involving flow in porous media, fifty percent or more of the original oil-in-plane is left in a typical oil reservoir by traditional recovery techniques. This unrecovered oil is a large target for enhanced or tertiary oil recovery methods now being developed [11].

Theoretical attempts to study the properties of porous media include continuum models and discrete models [11, 10, 49]. In the past twenty years ideas from the statistical physics of disordered media have been applied to flow, dispersion and displacement processes in porous rocks. These concepts include percolation theory [8], the natural language for describing connectivity effects and a variety of diffusion limited growth processes [50], which describe fundamentally nonequilibrium growth processes. Furthermore, use has been made of fractal concepts [6, 51], which are the main tool for describing the self-similarity and self-affinity of the morphology of a system and the effect of long-range correlations, and universal scaling laws, which describe how and under what conditions the effective macroscopic properties of a system may be independent of microscopic details. Scaling and fractal concepts provide powerful tools for describing flow, dispersion, and displacement processes in reservoir rocks [11].

Also, various experimental laboratory models have been developed in order to gain understanding in porous media problems [10]. In fluid flow experiments in porous media, the most easily tractable quantity is the height of the invading front. For example, Rubio *et al.* [25] have performed experiments where thin porous medium was made of tightly packed clean glass beads of various diameters. Water was injected into the porous medium to displace air in the system. The motion of the interface was recorded and digitized with high resolution. Hovárth *et al.* [26] have performed similar measure-

ments. This fact makes the dynamics of the interface between the invading and defending fluid of great interest.

A familiar example of this kind of a process is imbibition [52]. Take a paper sheet and place its bottom edge into water. Due to capillary forces, water starts to raise in the disordered fiber network. Initially, the water front is flat. As the invading front advances it starts to roughen. This kind of processes where an interface roughens in time are generally known as kinetic roughening [9]. Kinetic roughening of driven interfaces in random media is in fact a widely observed phenomenon in nature. In addition to being a theoretically interesting and challenging problem in non-equilibrium statistical physics, kinetic roughening has important applications in *e.g.* crystal growth [53] and fluid invasion in porous media [9].

In many cases of interest, there is a description of kinetic roughening processes in terms of a stochastic equation of motion for the (single-valued) height function $h(\vec{x}, t)$. The best known example is the Kardar-Parisi-Zhang (KPZ) equation [54]. For strongly driven interfaces, the stochastic noise term is usually uncorrelated in space and time, but in some cases it may also depend on h in which case the noise is quenched. The KPZ equation and its variants with different types of noise have been analyzed extensively [55, 56, 57, 58, 59, 60, 61, 62, 63, 64]. Another interesting and more recent class of problems concerns cases where the equation of motion for $h(\vec{x}, t)$ is *non-local* due to *e.g.* an underlying conservation law in the system [65, 66, 52]. For such cases, it's not generally possible to write down a local equation of motion. However, both classes of growth equations typically lead to algebraic scaling of the relevant height correlation functions, with associated scaling exponents whose values are known exactly in some special cases.

There are also growth models for which one cannot write an equation of motion for the single-valued height variable $h(\vec{x}, t)$. These include the directed percolation depinning model (DPD) [9, 67, 68] which is the pinned limit of the KPZ equation with quenched noise. For DPD, the interface roughness can be related to the geometric properties of the underlying directed percolation cluster. Also, there exist models in which the natural interface is multi-valued. Thus, if one defines a single valued height profile $h(\vec{x}, t)$ the overhangs play a significant role in the statistics of $h(\vec{x}, t)$. Example of such models include the lattice "forest fire" models [69, 70] and the diffusion limited aggregation model (DLA) [5] which has been of great importance in modeling of dendritic growt, dielectric breakdown and electrochemical deposition [71, 72]. For such cases there exists no theoretical explanation of the roughening properties of the interfaces at present.

The aim of the thesis is to study various static properties of random fractal clusters, networks produced by irreversible deposition processes, and dynamic properties of driven interfaces in fractal growth models. To this end, in Chapter 2 we first consider the fractal geometry of the Potts clusters at the critical temperature where a phase transition takes place. Most of the fractal dimensions D_S associated with the subsets S of the fractal clusters have exact predictions [18, 19, 20, 73]. These subsets include the total mass of the cluster, the hull, the external perimeter, the singly connected bonds and the gates to fjords. It is shown that the masses M_S of the subsets S, which determine the fractal dimensions D_S, approach the asymptotic behavior relatively slowly. Thus, for correct extrapolation of the fractal dimensions *corrections to scaling* terms have to be taken into account. Using renormalization group approach [74] and mapping to the Coulomb gas model [75], exact correction terms are derived. The predictions are tested against data from numerical simulations. For the fractal dimensions, good agreement with the theory is found, whereas for the correction terms, precise estimation of the correction parameters is impossible with the present range and quality of the data. However, good qualitative agreement with the predicted corrections is shown to hold. Next, we consider a class of deposition models which produce fractal structures. In Chapter 3, we introduce the so-called "rejection model" (RM), where there is an effective repulsive interaction between the deposited particles. RM models a deposition process where large equally charged molecules are deposited on surfaces with a tendency to repel each other. We present a detailed study of the percolation properties of the model as a function of the interaction parameter. We also study the spatial correlations within the networks formed. Geometric properties of fractal clusters play an important role in dynamics and kinetic roughening of single-valued fronts in fractals. In Chapter 4 we study three important growth models that produce fractals: invasion percolation, diffusion limited aggregation and ballistic deposition models. In particular, we show that starting from the distribution $P(\Delta h)$ of the nearest neighbor height differences Δh, which is shown to have a power-law decay form with decay exponent α, exponents governing the local scaling of the interfaces can be derived. Our results show that the fractal growth models exhibit intrinsic anomalous scaling and that the interfaces are multifractal. We compare our results with numerical simulations and find excellent agreement. Moreover, in the case of an isotropic fractal we derive an equation that connects the decay exponent α to the exponent describing bulk properties of the underlying fractal cluster. We also device an efficient simulation method for speeding up discrete random walks in disordered environments. Finally, summary and conclusions are presented in Chapter 5.

Chapter 2

Fractal Geometry of Potts Clusters

To familiarize the reader with the basic concepts needed to understand the rest of the present Chapter, we start by briefly reviewing the necessary quantities and definitions in Section 2.1. We then continue to present our results on fractal geometry of the Potts clusters in Section 2.2. We present the derivation of analytic results in Publication III in more detail here. These results are needed in the analysis of our unpublished numerical data [1].

2.1 Basic Concepts on Fractals

Let us consider a lattice model for a fractal, where each of the lattice sites can either be occupied or vacant, and let $\mathbf{r}_i$ denote the occupied sites. The most common measure of the spatial size of the cluster is the radius of gyration, R_s, which for a cluster of size s is defined as

$$R_s^2 = \sum_{i=1}^{s} \frac{|\mathbf{r}_i - \mathbf{r}_0|^2}{s} = \sum_{\mu=1}^{d} \left[s X_\mu^{(2)} + (X_\mu^{(1)})^2 \right], \tag{2.1}$$

where $\mathbf{r}_0 = \sum_{i=1}^{s} \frac{\mathbf{r}_i}{s}$ is the *center of mass* of the cluster. The latter form is convenient for practical purposes [76], with $X_\mu^{(\nu)}$ defining the ν^{th} moment for the μ^{th} coordinate, where $\mu = 1, \ldots, d$ and d is the spatial dimension. There are obviously other measures for the linear size of the cluster, but in practice R_s is found to give the best averaging when measuring quantities as a function of the cluster size.

To describe the shape of a fractal cluster, Cartesian geometry is not sufficient. Mandelbrot [15] introduced the concept of fractal geometry to distinguish between various fractals. Fractal geometry is defined by the dependence of the mass of cluster's subsets on the cluster size. Subsets of interest include the total mass (M) [77] of the cluster, the hull (H) [78] of the cluster, the external perimeter (EP) [79] of the cluster, the singly connected (SC) [80] sites of the cluster and the gates to fjords (G) [81].

For a fractal object, the mass M_S of the subset S is asymptotically, *i.e.* for large cluster size R, found to obey a power law

$$M_S \propto R^{D_s}, \tag{2.2}$$

where D_S defines the fractal dimension of subset S.

In practice, the asymptotic regime where the scaling of Eq. (2.2) holds, is often out of reach of computer simulations. To avoid misinterpretation of the measured data for $M_S(R)$, one thus needs to take into account the so called *corrections-to-scaling* terms that describe how the asymptotia is reached. An example of these is a power-law correction with exponent θ:

$$M_S \propto R^{D_s}(1 + AR^{-\theta}), \tag{2.3}$$

where A is a constant. For extrapolation of the data, we sometimes consider the local slopes $D_S^{\text{eff}}(R)$ of the data, which for the correction of Eq. (2.3) read as

$$D_S^{\text{eff}}(R) = \frac{d\log[M_S(R)]}{d\log R} \approx D_s - BR^{-\theta}, \tag{2.4}$$

where B is some other constant. To find $D_S^{\text{eff}}(R)$ one can e.g. perform a linear fit on a log-log scale to small subsets of the data around each value of R. One then tries several values of θ and plots the data against $1/R^{\theta}$. The value of θ that yields a straight line gives correct extrapolation of D_S to the $R \to \infty$ limit. The other possibility is to perform a non-linear fit to the parameters D_S, A, and θ. In some special cases, more than one correction terms have to be considered.

2.2 The Potts Model

A well known model to study the properties of magnetic materials is the q-state Potts model [7], defined through the Hamiltonian

$$\mathcal{H} = -K\sum_{\langle i,j\rangle}(\delta_{\sigma_i,\sigma_j} - 1), \tag{2.5}$$

where $\langle i,j\rangle$ denotes the summation over nearest neighbor sites i,j, the spin variable σ_i can take any of the values $1,2,\ldots,q$ and K is the thermal coupling with the factor $1/k_{\mathrm{B}}T$ absorbed in it. It is possible to extend q to real values [7], but here we shall concentrate here on the Potts model with integer values of q. In particular, we study Potts models with $q=1,2,3,$ and 4, where the thermal phase transition at the critical temperature $T_c = 1/\ln(1+\sqrt{q})$ [7] is of second order.

One defines the fractal clusters in the Potts model through the Fortuin-Kasteleyn [82] cluster decomposition, which states that the model can be mapped onto a general percolation model. The partition function

$$\mathcal{Z} = \mathrm{Tr}_\sigma e^{\mathcal{H}} \tag{2.6}$$

can be presented in terms of bond variables (a brief and clear re-derivation is presented in Ref. [22]). Let $p = 1-\exp(-K)$ denote the probability to form a bond between two nearest neighbor sites. Now, in a configuration with N_c clusters $\mathcal{Z}$ can be expressed as

$$\mathcal{Z} = \mathrm{Tr}_{\mathrm{bonds}} p^b (1-p)^n q^{N_c}, \tag{2.7}$$

where b is the number of bonds and n is the number of interactions that did not form a bond. Thus the problem of thermal lattice model can be mapped to a graph problem. The FK decomposition has been the starting point for efficient cluster algorithms [22, 23] for simulation of spin models. The fractal clusters one thus really takes a look at are those formed by nearest neighbor spins possessing the same spin value and connected by a bond.

The Potts model has been shown to exhibit rich critical behavior, and it has been related to a number of problems in lattice statistics [7]. Although of great theoretical interest in itself, it also has many experimental realizations. The 1-state Potts model is equivalent to a bond percolation problem [7], and the 2-state Potts model is the same as the Ising model [2]. The relevance of the absorbed monolayers in two-dimensional $q=3$ Potts model has been pointed out by e.g. Alexander [83] and Bretz [84]. Domany *et al.* [85] suggested that N_2 absorbed on krypton-plated graphite should exhibit a critical behavior as the $q=4$ Potts model. More references of the experimental realizations can be found in the review article by Wu [7].

Here we study geometrical aspects of the critical Potts clusters in two dimensions. This is in direct analogy with the geometry of percolation clusters, which has been widely studied [8, 18, 19, 86]. Specifically, we measure the fractal dimensions $D_M,\ D_H,\ D_{EP},$ and D_{SC} describing whether the scaling

of the cluster's mass, hull, external accessible perimeter [86], singly connected bonds [87] and the gates to *narrow-gate* fjords [19], respectively, with its radius of gyration R. As emphasized by Coniglio [73], many of these fractal dimensions have been derived analytically [18]. Some others have been found more recently [19, 20].

This Section starts with a description of numerical methods used in simulation of the Potts models in Section 2.3. Our numerical simulations show that the asymptotic power law dependence of the various masses on R is approached relatively slowly, and therefore the analysis of the data must include *correction terms*, particularly as q approaches 4. The theory developed to obtain these correction terms is explained in Section 2.4. Finally, we compare our numerical data with the exact predictions in Section 2.5. We note that while the analytical predictions can be found in Publication III, our numerical work presented here has not been published yet [1].

2.3 Simulation of Potts Clusters

2.3.1 Generating Potts Spin Configurations.

Numerical simulations of spin models have developed from local spin flip type algorithm [88] to more advanced cluster algorithms [22, 23]. Our simulations were done in 2D square lattice with both open and periodic boundary conditions. Clusters of the q-state Potts model were generated using the Swendsen-Wang algorithm [22], which is based on the cluster decomposition by Fortuin and Kasteleyn [82]. The size of the system in our simulations was 4096^2 spins for all q. In Figure 2.1, we show sample clusters for different values of q.

2.3.2 Thermalization

All simulations were started with a homogeneous initial condition, with all spins initially parallel to each other. First we thermalized the system to allow the model to equilibriate. Thermalization was checked by measuring both the energy per spin e directly from the Potts Hamiltonian and magnetization per spin m using the representation of Potts spins in a $q-1$ dimensional space [7].

Thermalization of large spin systems takes a very long time. The quantities of interest in this work show a relatively slow approach to the asymptotic values.

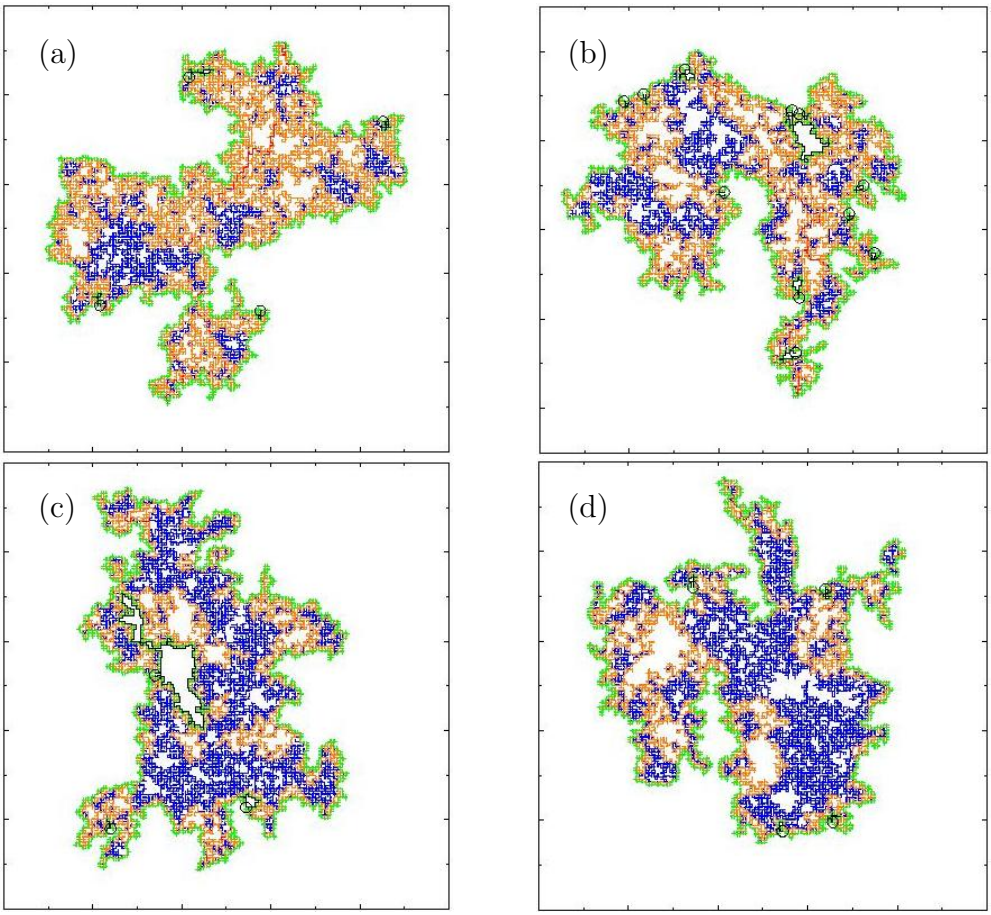

Figure 2.1: Computer generated Potts clusters for (a) $q = 1$, (b) $q = 2$, (c) $q = 3$ and (d) $q = 4$ state Potts models. Colors indicate different subsets: SC bonds are shown in red, H bonds are shown in yellow and the rest of the bonds contributing to M are shown in blue. The EP bonds are colored green and the gates to fjords are marked by black circles, while the fjord is shown with a black line.

Thus, extremely large lattices are required to to analyze the scaling behavior of the cluster subset masses. When performing simulations on lattices of size $L = 2^{12} = 4096$, about 20000 Monte Carlo steps (lattice sweeps) are needed to equilibrate the system.

In this work, a simple method was developed to overcome this problem. Small lattices thermalize quickly so we started with a small one of size L_1 and thermalized it. We then periodically copied the spin configuration of the small lattice to a lattice with twice as large a size $L_2 = 2 \times L_1$ and thermalized

it. We continued this process until the desired system size was reached. In practice, it is recommended to compare the values of e and m obtained this way with the values obtained from conventional thermalization to be sure that the system really is thermalized. Alternatively, one can continue running the simulation and collect the values of thermodynamical variables as a function of time and check that there is no increasing or decreasing trend in them. The thermalization method described above allows a speed-up by an order of magnitude in thermalization for a Potts spin system of 1024^2 spins.

2.3.3 Measuring the Cluster Subsets

After the spin system was thermalized, we took samples of the cluster configurations after every 20 spin updates (corresponding to the correlation time for the present system sizes) to get uncorrelated samples. Each spin cluster of the present configuration was taken separately under investigation. However, as a precaution to avoid some of the finite size effects, we collected the data from only those clusters which did not involve spins on the boundary.

For the remaining clusters we determined the masses of the cluster subsets as explained in Appendix A. Since any thermalized spin configuration contains clusters of many sizes, we collected the data in multiplicatively increasing bins of the size of the cluster. Each bin contained the clusters of sizes $[R_i, R_{i+1} = \sqrt{2}\ R_i]$.

2.4 Corrections to Scaling

Our numerical results on the cluster subset masses $M_S(R)$ reveal that there is complicated finite size scaling present, and that the asymptotic power law dependence of the masses on R is approached relatively slowly. Therefore, corrections-to-scaling terms have to be taken into account in the data analysis for correct extraction of the fractal dimensions. Below we present the analytic results that can be obtained starting with the renormalization group approach as discussed in Publication III. Next, we consider the mapping of the Potts model on to the Coulomb gas model. Finally, we discuss the so called "analytic corrections" and summarize the theory.

2.4.1 Renormalization Group

Experimentally [24] a variety of surface adsorbate systems with phase transitions, which provide realizations [7] of various Potts models, have been studied. In such experimental systems the coverage can vary leading to the study of Potts lattice gases in which a dilution field ψ (describing the lattice sites are vacant or occupied by the spins) enters in a natural way. Nienhuis *et al.* [89] proposed a renormalization procedure in which disordered spin cells of a pure Potts model were mapped onto vacancies and found that the dilution field plays an essential role. Nauenberg and Scalapino [90] proposed a set of differential renormalization equations for the temperature and the dilution fields. The work was further extended by Cardy *et al.* [74] and a theory of the scaling behavior near $q_c = 4$ was developed.

The physical variable space of the dilute Potts model depends upon the number of Potts states q, the temperature, the ordering field and the concentration [74]. The renormalization group equations can be expressed in terms of universal parameters when scaling fields are used. The scaling fields are analytically related to the physical variables, which are called ϕ, h, and ψ which denote the thermal, ordering and dilution fields, respectively. Making the fundamental assumption of analyticity, it is found [74] through second order in ψ or $\sqrt{-\epsilon}$, where $\epsilon = q - 4 \leq 0$ that under an infinitesimal scale change $d\ell$

$$\frac{d\psi}{d\ell} = a(\psi^2 + \epsilon), \tag{2.8}$$

$$\frac{d\phi}{d\ell} = (y_T + b\psi)\phi, \tag{2.9}$$

$$\frac{dh}{d\ell} = (y_H + c\psi)h. \tag{2.10}$$

Here, a, b, c, y_T and y_H are universal parameters that can be obtained by comparison with other known results [74]. From this set of equations, the authors of Ref. [74] derive the physical properties, such as logarithmic temperature corrections to the specific heat for the Potts lattice gas for q near 4. In the $q = 4$ case, logarithmic corrections for the susceptibility are obtained in Ref. [91] using similar approach. We now describe how the renormalization group recursion relations (RGRR's) can be generalized to study the corrections to scaling for the various cluster subsets.

The correction terms that can be derived from Eqs. (2.8) and (2.10) relate to the *dilution field* ψ which is generated under renormalization even when one starts with the non-dilute case [74]. For our non-dilute case, one expects

$\psi(\ell)$ to increase under RGRR's from $-\infty$ towards its critical value ψ^* (≤ 0 for $q \leq 4$), while the cluster linear size like all other lengths rescales as $R(\ell) = Re^{-\ell}$. Following Cardy *et al.* [74], we assume that ℓ_0 preceding iterations bring ψ from $-\infty$ up to $\psi(\ell_0) = \psi_0$, with $|\psi_0| \ll 1$. To obtain also higher order corrections, we write Eq. (2.8) to higher order in ψ and $\epsilon = q - 4$ (ψ^2 is of the order of ϵ) to obtain

$$\frac{d\psi}{d\ell} = a(\epsilon + \psi^2 + b\psi^3 + r\epsilon\psi + ...). \tag{2.11}$$

At $q = 4$, this yields

$$a(\ell - \ell_0) \approx \psi_0^{-1} - \psi(\ell)^{-1} + b \log \frac{b + \psi(\ell)^{-1}}{b + \psi_0^{-1}}. \tag{2.12}$$

Iterating up to $R(\ell^\times) = 1$, we can express $\psi(\ell^\times)$ in terms of $\log R = \ell^\times$. For large R, $\psi_0/\psi(\ell^\times) \approx A(\log R + B \log(\log R) + E) + \mathcal{O}(\log\log R/\log R)$, where $A = -a\psi_0,\ B = -b/a$ and E also depends on $a,\ b,\ \ell_0$ and ψ_0.

For $q < 4$, an expansion to second order in $\epsilon' = \sqrt{-\epsilon}$ yields $\psi(\ell^\times) \approx \psi^* + \tilde{B}R^{-\theta}$, with $\psi^* = -\epsilon'[1 - (r - b)\epsilon'/2] + \ldots$, $\theta = 2a\epsilon'(1 - b\epsilon') + \ldots$ and $\tilde{B} \propto (\psi_0 - \psi^*)$. To order $-\epsilon'$, one obtains a full solution,

$$\psi(\ell) = -\epsilon' \frac{1 + \hat{B}e^{-\theta\ell}}{1 - \hat{B}e^{-\theta\ell}}, \tag{2.13}$$

where $\hat{B} = (\psi_0 + \epsilon')/(\psi_0 - \epsilon')$. Indeed, ψ approaches ψ^* for large ℓ.

To obtain the scaling of $M_S(R)$, we generalize Eq. (2.10) and write the RGRR for the field h_S conjugate to the density $\rho_S \equiv M_S/R^d$ as

$$\frac{dh_S}{d\ell} = [y_S + c_S\psi(1 + e_S\psi + f_S\psi^2 + \ldots)]h_S, \tag{2.14}$$

where the coefficients may depend on ϵ. ρ_S is then found as a derivative of the free energy with respect to h_S. For $q = 4$, its singular part becomes

$$\begin{aligned} \rho_S(\ell) &\propto e^{-d\ell} h_S(\ell)/h_0 \\ &= \exp[(y_S - d)\ell + \int_{\ell_0}^{\ell} \{c_S\psi(1 + e_S\psi + f_S\psi^2 + \ldots)\} d\ell] \\ &\propto e^{(y_S - d)\ell} [\psi(\ell)/\psi_0]^{c_S/a} (1 + \mathcal{O}(\psi(\ell)). \end{aligned} \tag{2.15}$$

For large $\log R = \ell^\times$, this becomes

$$M_S \propto R^{D_S} (\log R + B \log(\log R) + E)^{-c_S/a} (1 + \mathcal{O}(\log\log R/\log R)), \tag{2.16}$$

with $D_S = y_S(q=4)$, and c_S/a is to be taken from Table 2.1 (see below). Note that $B = -b/a$ is universal (i.e. independent of ψ_0), and the non-universal constant E is the same for all S. Equation (2.16) generalizes the logarithmic corrections of Cardy *et al.* [74].

In practice, the numerical results are often analyzed by looking at the local logarithmic slope,

$$\begin{aligned} D_S^{\rm eff} &= d\log M_S/d\log R = d\log h_S/d\ell|_{\ell=\ell^\times} \\ &= y_S + c_S\psi(\ell^\times)[1 + e_S\psi(\ell^\times) + f_S\psi(\ell^\times)^2 + \ldots]. \end{aligned} \tag{2.17}$$

In some cases, this expression (in which $\psi(\ell^\times)$ is related to $\log R = \ell^\times$ via Eq. (2.12)) gave a better fit than the derivative of the approximate expression in Eq. (2.16).

For $q < 4$, to leading order in ϵ' the same procedure turns Eq. (2.13) into

$$M_S \propto R^{D_S}(1 - \hat{B}R^{-\theta})^{-c_S/a} \approx R^{D_S}(1 + f_S R^{-\theta}), \tag{2.18}$$

where $D_S \approx y_S - c_S\epsilon'$ and $\theta \approx 2a\epsilon'$. The RHS of this equation remains correct also for higher orders in ϵ'. Note that to the lowest order in ϵ', the ratios $f_S/f_{S'}$ are universal, being equal to $c_S/c_{S'}$. This is similar to analogous ratios for thermodynamic properties in the usual ϵ-expansion [92]. Expanding the exact D_S (Table 2.1) in ϵ' yields c_S. Using also $a = 1/\pi$ (see below) yields our predictions for c_S/a (given in Table 2.1), to be used in fitting Eq. (2.16). The form on the RHS of Eq. (2.18) is already implied by den Nijs [75], who found that the pair correlation functions $G_H(r)$ can be expanded as a sum over r^{-2x_n}, where x_1 is the leading exponent, implying a leading correction exponent

$$\theta = 2(x_2 - x_1) = 4(4-g)/g. \tag{2.19}$$

The q-dependent coupling constant g is defined through [18]

$$q = 2 + 2\cos(\pi g/2). \tag{2.20}$$

Thus, for $q = 1, 2, 3$ and 4, $g = 8/3, 3, 10/3$ and 4. Expanding the expression of Eq. (2.19) in powers of ϵ' yields the coefficients $a = 1/\pi$ and $b = -1/2\pi$, which we use in our fits to Eq. (2.12). The value $a = 1/\pi$ also agrees with Cardy *et al.* [74]. This expression for θ also reproduces known results for $q = 2, 3$, as listed in Table 2.1.

2.4.2 Coulomb Gas

The second source of corrections involves new contributions to the relevant pair correlation functions in the Coulomb gas representations [75]. In some of

the exact derivations, the q-state Potts model renormalizes onto the vacuum phase of the Coulomb gas, involving "particles" with electric and magnetic "charges" (e, m). At criticality, the corresponding Coulomb gas has a basic "charge" $\phi = |2 - g/2|$ mod 4. Various Potts model two-point correlation functions $G_S^P(\vec{r})$ are then mapped onto Coulomb gas analogs, which give the probability of finding two charged particles at a distance r apart. Asymptotically, these are given by

$$G^{CG}_{[(e_1,m_1),(e_2,m_2)]}(\vec{r}) \propto r^{-2x^{CG}_{[(e_1,m_1),(e_2,m_2)]}}, \tag{2.21}$$

where

$$x^{CG}_{[(e_1,m_1),(e_2,m_2)]} = -\frac{e_1 e_2}{2g} - \frac{g m_1 m_2}{2}. \tag{2.22}$$

Hence one identifies $D_S = d - x^{CG}_{[(e_1,m_1),(e_2,m_2)]}$, with $d = 2$. The results in Table 2.1 for $S = M$ were obtained by den Nijs [75], who noted that the spin-spin correlation function of the Potts model maps onto a Coulomb gas total electric charge $Q = -2\phi$, which splits into the two charges $e_{1,2} = \pm 1 - \phi$ (and $m_{1,2} = 0$). Continuing along similar lines, Saleur and Duplantier [18] used a mapping onto the body-centered solid-on-solid model, requiring a vortex-antivortex pair with $e_{1,2} = -\phi$ and $m_{1,2} = \pm 1/2$ or ± 1 for the fractal dimensions of $S = H$ or $S = SC$. The Table also contains Duplantier's recent result [20] for $D_{EP} = 2 - x^P_{EP}$, which has not been expressed in terms of Coulomb charges. The results for x^P_H and x^P_{SC} are special cases of the expression $x_\ell = g\ell^2/32 - (4-g)^2/(2g)$, with $\ell = 2$ and 4, respectively [18]. For percolation ($q = 1$ and $g = 8/3$), this expression also yields $x^P_{EP} = x_3 = 2/3$ for the external perimeter and $x^P_G = x_6 = 35/12$ for the gates to fjords [19].

We now turn to corrections to the leading behavior. M. den Nijs [75] derived such corrections for the order parameter correlation function. In that case he noted that the charge $Q = -2\phi$ could also split into the pair $e_{1,2} = \pm 3 - \phi$, yielding a contribution to G^P_M of the form $r^{-2x^P_{M,2}}$, with $x^P_{M,2} = x^{CG}_{[(3-\phi,0),(-3-\phi,0)]} = x^P_M + 4/g$. Since $D = d - x$ usually represents a fractal dimension, we relate each of these correction terms to some subset of the cluster, with dimension $D_{M,2} = 2 - x^P_{M,2} = D_M - 4/g$. Writing M_M as a sum of powers R^{D_i}, [93, 94] we have $M_M \propto R^{D_M}(1 + f' R^{-\theta'})$, with $\theta' = 4/g$.

As far as we know, there has been no discussion of the analogous corrections to the other subsets discussed here. In the spirit of den Nijs [75], we note that the correlation function for both H and SC could also result from electrical charges $e_{1,2} = \pm 2 - \phi$, instead of $-\phi$. For both of these cases this would give $x' = x + 2/g$, hence a correction exponent $\theta'' = 2/g$. At the moment, there exists no theory for corrections to M_{EP}. However, in the spirit of the renormalization group it is also reasonable to interpret θ' and θ'' as the scaling

exponent of some irrelevant perturbation (yet to be identified). If that were true then we might expect the same perturbation also to affect other quantities, such as M_{EP}. This conjecture is supported by the "superuniversal" relation $(D_H - 1)(D_{EP} - 1) = 1/4$ found by Duplantier [20]. If this relation also holds for the effective dimensions (as happens e.g. in the ϵ-expansion [92]), then H and EP should have the same correction exponents.

2.4.3 Analytic Corrections

The last source of corrections involves "analytic" terms, coming e.g. from linear cuts with dimensions $(D_S - 1)$ [93, 94] or from replacing R by $(R + a)$, since there are many possible candidates for the correct linear measure of the cluster. These would imply corrections of relative size of $1/R$.

Combining all of these sources, we end up with the prediction (for $q < 4$)

$$D_S^{\text{eff}} = D_S + \sum_i f_i R^{-\theta_i}, \tag{2.23}$$

with $\theta_i = \theta,\ \theta'$ (or θ'') and 1.

In the $q = 4$ case, there are both logarithmic and power law corrections, since the Coulomb gas approach gives $\theta' = 1/2$ and $\theta'' = 1$ in addition to the logarithmic corrections coming from the renormalization group theory.

2.5 Numerical Results

We present the numerical data from large scale Monte Carlo simulations of the Potts models. Our aim is to confirm the exact predictions of the fractal dimensions D_S in the cases where they are available and to give numerical estimates for the exponents that have not yet been calculated exactly. In addition, we want to numerically confirm the corrections-to-scaling theory presented in the previous section.

We obtain good agreement with the theoretically predicted values for most of the fractal dimensions D_S. The worst agreement is found for the exponent of external perimeter D_{EP} for $q > 2$ Potts models. The reasons for this will be discussed below. However, fixing the correction terms and performing fits only to the amplitudes and fractal dimensions D_S of Eqs. (2.17) and (2.23), yielded estimates for the subset fractal dimensions that agree to the precision of 0.05 or better with the theoretical predictions of Table 2.1.

	D_S	$q=1$	$q=2$	$q=3$	$q=4$	c_S/a
S		$\frac{8}{3}$	3	$\frac{10}{3}$	4	
M	$(g+2)(g+6)/(8g)$	$\frac{91}{48}$	$\frac{15}{8}$	$\frac{28}{15}$	$\frac{15}{8}$	$\frac{1}{16}$
H	$1+2/g$	$\frac{7}{4}$	$\frac{5}{3}$	$\frac{8}{5}$	$\frac{3}{2}$	$-\frac{1}{4}$
EP	$1+g/8$	$\frac{4}{3}$	$\frac{11}{8}$	$\frac{17}{12}$	$\frac{3}{2}$	$\frac{1}{4}$
SC	$(3g+4)(4-g)/(8g)$	$\frac{3}{4}$	$\frac{13}{24}$	$\frac{7}{20}$	0	-1
θ	$4(4-g)/g$	2	$\frac{4}{3}$	$\frac{4}{5}$	0 (log)	
θ'	$4/g$	$\frac{3}{2}$	$\frac{4}{3}$	$\frac{6}{5}$	1	
θ''	$2/g$	$\frac{3}{4}$	$\frac{2}{3}$	$\frac{3}{5}$	$\frac{1}{2}$	

Table 2.1: Exact theoretical predictions for the fractal dimensions and corrections to scaling terms in the q-state Potts models. Subsets S are defined in Sec. 2.2, and the q-dependent coupling constants g in Sec. 2.4.

We are not able to give a quantitative numerical proof of the values predicted for the correction terms. Qualitatively, our numerically evaluated functions $M_S(R)$ display complex corrections-to-scaling behavior that requires more than one correction term. The theoretical predictions can be fitted reasonably well to the data keeping the important quantities such as θ, θ' (or θ'') and c_S/a fixed while leaving the amplitudes of individual correction terms free.

We start this section by studying the fractal geometry of clusters in the site percolation model, which is computationally easier to simulate. The reasons behind the difficulties in comparison of the numerical data with the analytical predictions are discussed. We then proceed to present our numerical data on the Potts clusters. We note that in all the figures of this Chapter the error bars are smaller the size of the symbols if not shown explicitly.

2.5.1 Site Percolation Clusters

The simulations were done on a square lattice of size 24576^2 using the Ziff-Newman cluster labeling [95], which is an improved version of the Hoshen-Kopelman algorithm [96]. Thus the linear lattice size was 6 times larger than in the simulation of Potts clusters.

To get a feeling of what kind of problems are present in the fitting procedure

when the theoretically predicted correction terms of Eqs. (2.18) and (2.16) are fitted to the numerical data on the cluster subset masses $M_S(R)$, let us consider as an example the scaling of the number of singly connected bonds. Figure 2.2 illustrates the scaling of $M_{SC}(R)$ with the cluster size R on a double logarithmic scale. The solid line indicates the fit to the data yielding an estimate for the asymptotic fractal dimension D_S, which is less than 0.01 off the exactly known value $D_{SC} = 3/4$.

Although the asymptotic scaling regime $M_{SC}(R) \propto R^{D_{SC}}$ can be seen here, there are difficulties in the extraction of the correction terms of Eq. (2.18). The smallest values of R included in the fit in Fig. 2.2 correspond to the regime where the influence of the correction terms are about to vanish, as can be seen in the inset of Fig. 2.2 where data are scaled with the predicted asymptotic behavior $M_S(R)/R^{D_S}$. On this scale, one sees that the data start to saturate to the asymptotics at $R \approx 300$. However, at the same point the statistics becomes so noisy that a precise estimation of the correction terms becomes difficult.

An additional difficulty arises from the fact that the finite size of the lattice is not taken into account in any way in the finite size scaling form of Eq. (2.18). Due to the finite system sizes, statistics of the large cluster is biased in such a way that only the compact clusters fit in the lattice without touching the boundaries. The extended clusters having for example more EP sites than compact clusters with the same radius of gyration R, are absent. This bias cannot be taken into account by any known correction terms. We tried to extrapolate the data from different system sizes to obtain an asymptotic curve for an infinitely large system, but the statistics is far from sufficient for such a procedure.

2.5.2 Potts Clusters

In the case of Potts clusters, system sizes that can be used in the simulations are much smaller (4096^2 spins) than those in the site percolation case, since in addition to the spin variables, also bonds must be stored. This causes the finite size effects to be even more pronounced than those present in the site percolation model simulations. In addition, the correction exponents in the $1 < q < 4$ Potts models are smaller than those in the $q = 1$ case. Also, the logarithmic corrections present in the 4-state Potts model are weaker than any of the power law corrections in $q < 4$ models. Thus, the influence of the corrections-to-scaling terms extends to much larger values of R.

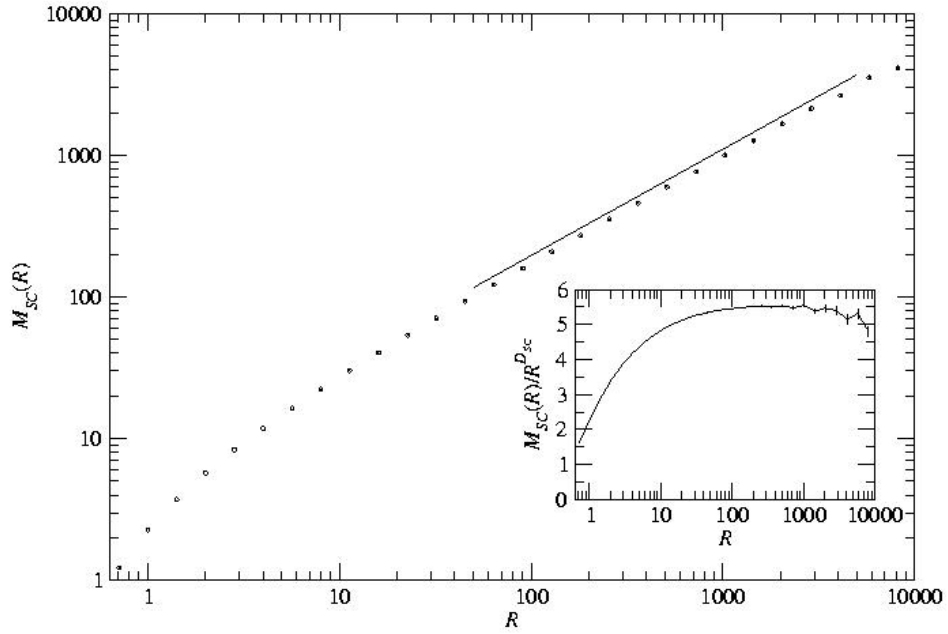

Figure 2.2: Site percolation model. The number of the singly connected bonds $M_{SC}(R)$ vs. the cluster size R. The predicted slope $D_{SC} = 3/4$ is indicated by the solid line. The inset shows the scaled mass $M_{SC}(R)/R^{D_{SC}}$. Note the saturation to the asymptotic scaling at $R \approx 300$.

The data analysis was done by fitting the theoretical predictions of Sect. 2.4 to the data. The nonlinear fitting was done using the Levenberg-Marquardt method [97]. Let $\mathbf{y} = \mathbf{y}(\mathbf{x}; \mathbf{a})$, where $\mathbf{a}$ is the parameter vector, be the model the data are fitted to. In addition, let y_i be the data measured at points x_i. The measure for the quality of fits χ^2 is defined through

$$\chi^2(\mathbf{a}) = \frac{1}{N_f} \sum_{i=1}^{N} [\frac{y_i - y(x_i; \mathbf{a})}{\sigma_i}]^2, \tag{2.24}$$

where the normalization factor N_f is the number of degrees of freedom and σ_i is the estimated error at point x_i. We determided the error bars of the fractal dimensions by fixing D_S to a range of values around the theoretically predicted one and performing a fit to the amplitudes. When the value of χ^2 exceeded 2, the range of D_S was closed. One can perform the fit directly to

$M_S(R)$, or to the effective fractal dimensions $D_S^{\rm eff}(R)$ (see Eq. (2.23) and Eq. (2.17)).

We found that for $q < 4$, fitting directly to the mass worked out better. To avoid problems with numerical accuracy the data was divided with the asymptotic behavior. Thus, for $q < 4$, the fits are done to the form

$$M_S/R^{D_S} = E(1 + f_S R^{-\theta} + f'_S R^{-\theta'} + g/R), \tag{2.25}$$

where E, f_S, f'_S, g, θ and θ' are the fitting parameters, and the fractal dimensions D_S are kept fixed.

In the $q = 4$ case, on the other hand, we found the fitting to the effective exponent $D_S^{\rm eff}$ better, and the fits were thus done to

$$\begin{aligned} D_S^{\rm eff} &= d\log M_S/d\log R \\ &\approx D - \frac{c_S/a(B + C + \log R)}{(C + \log R)(E + \log R + B\log(C + \log R))} \\ &\quad + Z/\log R. \end{aligned} \tag{2.26}$$

Note that we have added an additional constant C to the logarithmic derivative of Eq. (2.16). Also, the logarithmic derivative of the higher order term on the RHS of Eq. (2.16) was approximated by a simpler form $1/\log R$. In the fitting procedure, the possibility of having many candidates for the correct linear measure of the cluster size was taking into account by allowing R to adjust to $R + a$ (see Sect. 2.4).

In addition to fitting the $D_S^{\rm eff}(R)$ we tried fitting to Eq. (2.17), where the effective exponents $D_S^{\rm eff}(\psi)$ are related to the dilution field $\psi(\ell^\times)$ via $\log R = \ell^\times$ and in some cases this gave better fits than the approximate expression of Eq. (2.26). Here, $\psi(\ell^\times)$ was solved numerically from R.

Below, the resuts of our numerics are summarized for the various subsets. We do not consider numerical estimates for the various amplitudes in the nonlinear fits nor the fitting to the correction exponents and the parameters c_S/a as the present range and quality of data does allow accurate estimation of these quantities. Instead, we keep the correction terms fixed and try to extrapolate the fractal dimensions D_S, and to demonstrate that the predicted forms of scaling in Eqs. (2.26) and (2.25) are in good agreement with our numerical data.

Mass

Fig. 2.3 shows an example of the fit to the curve $M_M(q = 3)/R^{D_M}$. In the fitting procedure, D_M, θ and θ' were kept fixed while E, $f_M, f_{M'}$ and g were

allowed to fit. The value $\chi^2 = 1.17$ indicates that the data fits very well to the model of Eq. (2.25). Estimates for the subset fractal dimensions were done as follows. In all fits for $1 \leq q < 4$, θ and θ'' of Eq. (2.25) were kept fixed (at the predicted values), while the amplitudes of each correction term were allowed to adjust. In the $q = 4$ case, only c_M/a was fixed in Eq. (2.26). Our numerical estimates for the fractal dimensions $D_M(q)$ are 1.90 ± 0.01, 1.87 ± 0.01, 1.85 ± 0.02 and 2.05 ± 0.15 for $q = 1, 2, 3, 4$, respectively. These are in good agreement with the theoretical predictions.

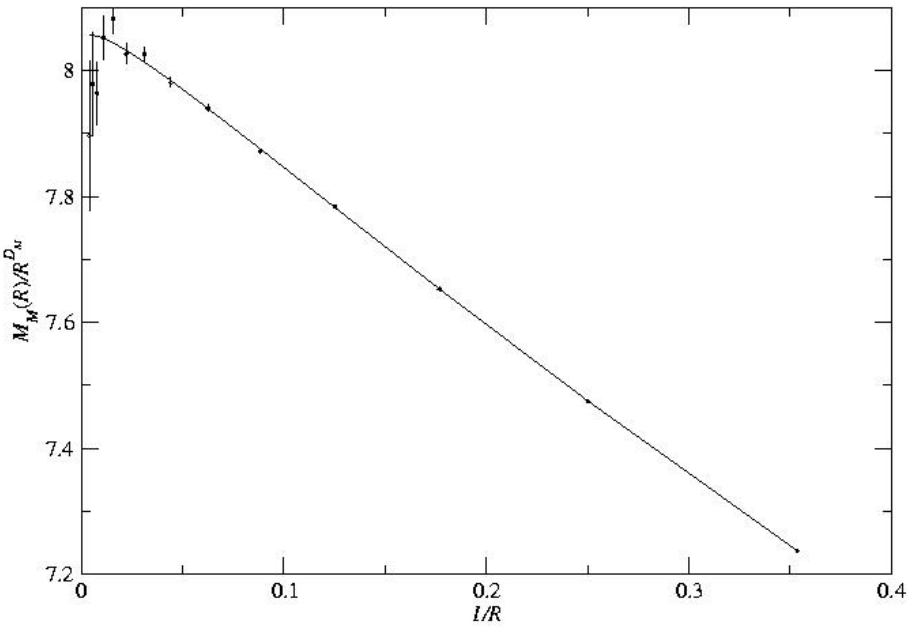

Figure 2.3: Total mass of the cluster mass M_M in the 3-state Potts model. Solid line is the nonlinear fit to the data. For this particular fit $\chi^2 = 1.17$.

Hull

Figure 2.4 shows a fit to the number of the bonds belonging to the hull in the $q = 4$ Potts model. In this particular fit, D_H and c_H/a were kept fixed while B, C, Z and a were free to adjust. The value of $\chi^2 = 1.11$ indicates

that the data fits well to the model of Eq. (2.26). In all fits for $1 \leq q < 4$, θ and θ' of Eq. (2.25) were kept fixed (at the predicted values), while the amplitudes of each correction term were allowed to change. In the $q = 4$ case, only c_H/a was fixed in Eq. (2.26). Our numerical estimates for the fractal dimensions $D_H(q)$ are 1.75 ± 0.01, 1.66 ± 0.01, 1.59 ± 0.03 and 1.50 ± 0.01, for $q = 1, 2, 3, 4$, respectively. Agreement with the theoretical predictions is excellent as can be seen by comparison with the values in Table 2.1.

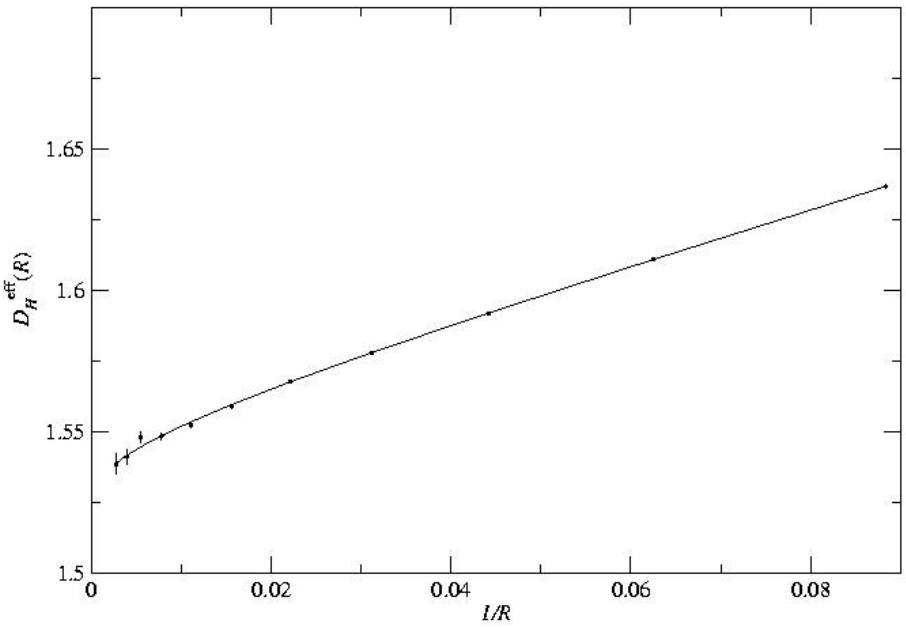

Figure 2.4: Effective exponent $D_H^{\rm eff}(R)$ against $1/R$ in the $q = 4$ Potts model. For this fit indicated by the solid line $\chi^2 = 1.11$.

External Perimeter

Figure 2.5 shows an example of the fit to the external perimeter data in the $q = 1$ Potts model. The fractal dimension D_{EP} and the correction exponents θ and θ' were kept fixed to the predicted values while B, C, Z and a were free to adjust yielding $\chi^2 = 1.69$, implying a reasonably good agreement

with the model of Eq. (2.25). Again, in the fits for $q < 4$, θ and θ' of Eq. (2.25) were kept fixed and in the $q = 4$ case, c_{EP}/a was fixed. The numerical estimates 1.33 ± 0.05, 1.36 ± 0.02, 1.40 ± 0.15 and 1.48 ± 0.02 for $q = 1, 2, 3, 4$, respectively, agree with the exact predictions.

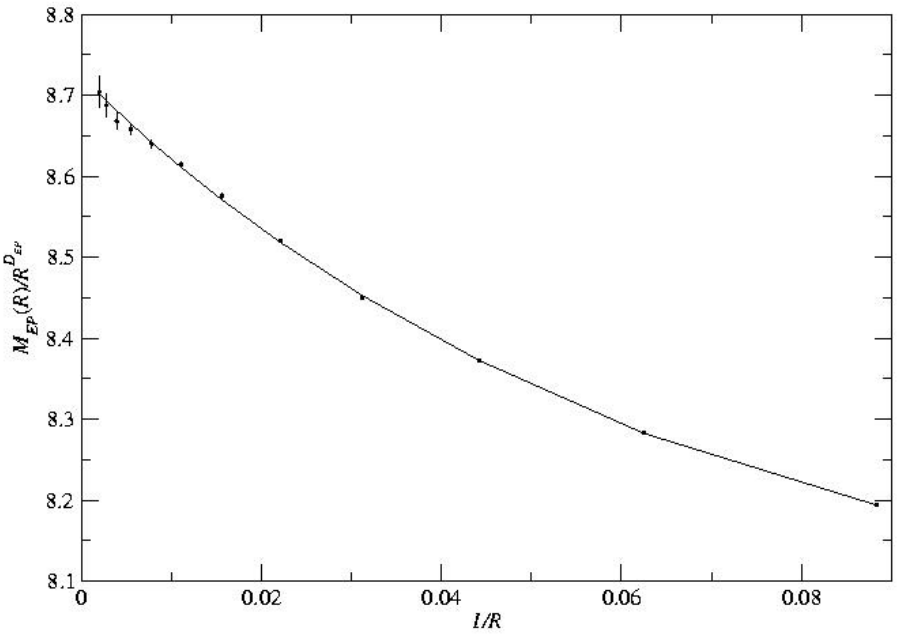

Figure 2.5: Number of the external perimeter bonds, M_{EP} versus $1/R$ in the $q = 1$ Potts model. Solid line indicates the fit to the data ($\chi^2 = 1.69$).

Singly connected bonds

In Fig. 2.6, we show the number of singly connected bonds $M_{SC}(R)/R^{D_{SC}}$ against the cluster size R in the $q = 2$ Potts model. The fractal dimension D_{SC} and the correction exponents θ and θ' were kept fixed to the predicted values while E, $f_{SC}, f_{SC'}$ and g were allowed to fit. The value $\chi^2 = 1.21$ implies good agreement with the model of Eq. (2.25) The numerical estimates for the fractal dimensions are 0.75 ± 0.02, 0.55 ± 0.03, 0.35 ± 0.07 and 0.03 ± 0.08 for $q = 1, 2, 3, 4$, respectively. All the estimates for the fractal dimensions

D_{SC} are in good agreement with the theoretical predictions. However, the large value of $\chi^2 \approx 3$ in the $q = 4$ case indicates some discrepancy between the model of Eq. (2.26) and the data.

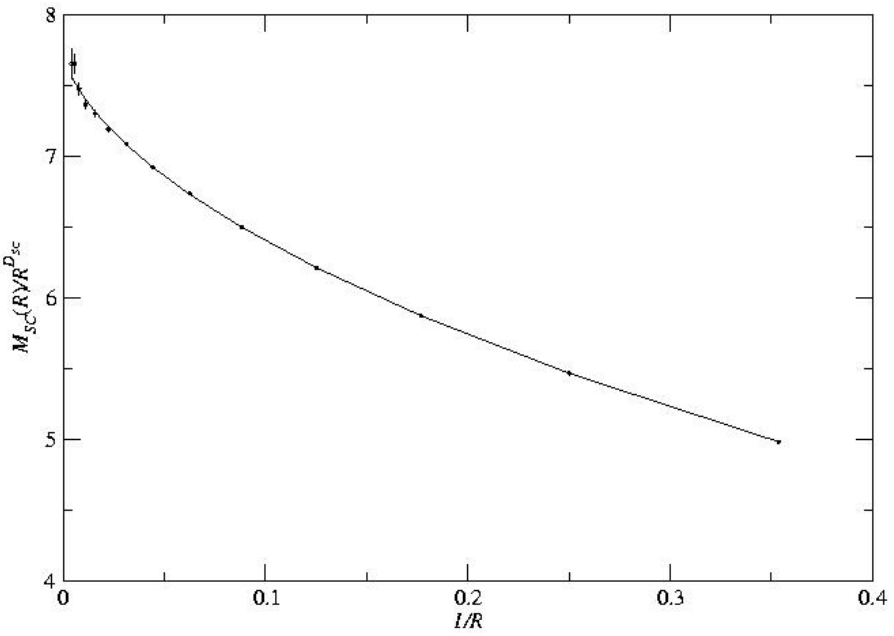

Figure 2.6: Number of the singly connected bonds M_{SC} against $1/R$ in the $q = 2$ Potts model. Solid line is the nonlinear fit for which $\chi^2 = 1.21$.

Gates to Fjords

Figure 2.7 shows our numerical data for the number of gates to narrow-gate fjords. In the Figure, fits to the data along with the estimates for the fractal dimensions D_G are shown. Our estimate $D_G(q = 1) = -0.9 \pm .05$ agrees well with the exact prediction $D_G = -11/12 \approx -0.92$ [19]. Here, only a linear fit to the data on the double logarithmic scale was considered, since the scaling regime for the presently available cluster sizes is rather narrow. Our numerical estimates of all the fractal dimensions are summarized in Table 2.2.

The parameter s governing the minimal ratio of the fjord size to the cluster size that we used was in the range $0.1 \leq s \leq 0.2$. The actual choice for the value of s does not affect the scaling law, but it merely determines the range where the power law behavior $M_G \sim R^{D_G}$ starts (decreasing s shifts the maximum of the curves $M_G(R)$ to the left).

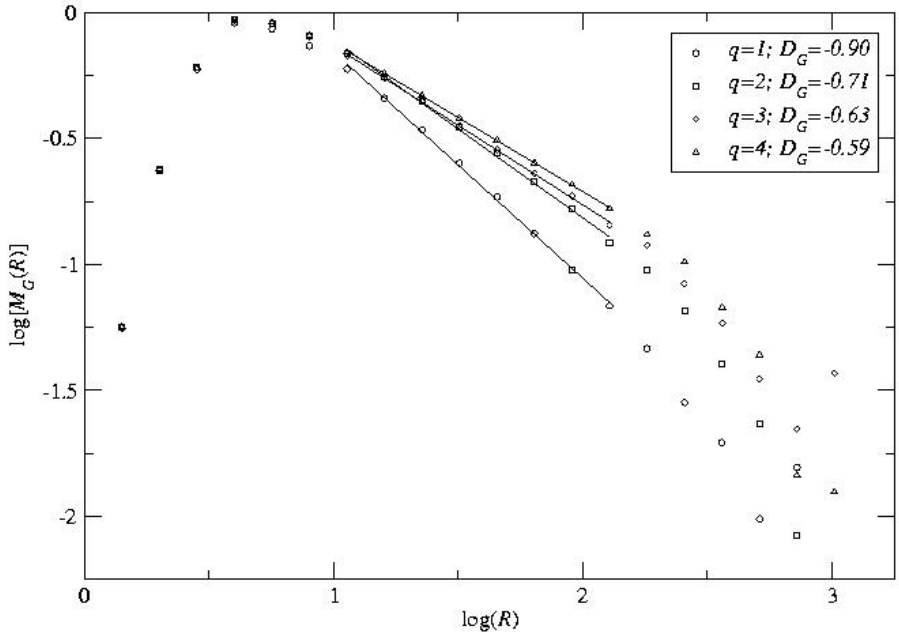

Figure 2.7: Data on the $M_G(R)$, the number of gates to fjords on log-log scale. Different values of q are represented by the symbols shown in the legends. Straight lines indicate the fits to the data; slopes give the exponents D_G.

Summary of Numerics

To summarize, in the comparison between theory and numerics, extreme caution is needed in the extraction of the fractal dimensions D_S from the numerical data. The corrections-to-scaling theory presented in the previous section already implies that the finite size effects arising from the finite cluster

size are strong. In addition, effects coming from the finite lattice size lead to an uncontrollable bias that is very difficult to handle. The difficulties are most pronounced in the case of SC and EP as q approaches 4. Taking the correct finite size scaling terms as given in Eqs. (2.25) and (2.26), improves the estimates of the fractal dimensions, but some discrepancies remain.

S	$D_S(q=1)$		$D_S(q=2)$		$D_S(q=3)$		$D_S(q=4)$	
	n	e	n	e	n	e	n	e
M	1.90(1)	$\frac{91}{48}$	1.87(1)	$\frac{15}{8}$	1.85(2)	$\frac{28}{15}$	2.05(15)	$\frac{15}{8}$
H	1.75(1)	$\frac{7}{4}$	1.66(1)	$\frac{5}{3}$	1.59(3)	$\frac{8}{5}$	1.50(1)	$\frac{3}{2}$
EP	1.33(5)	$\frac{4}{3}$	1.36(2)	$\frac{11}{8}$	1.40(15)	$\frac{17}{12}$	1.48(2)	$\frac{3}{2}$
SC	0.75(2)	$\frac{3}{4}$	0.55(3)	$\frac{13}{24}$	0.35(7)	$\frac{7}{20}$	0.03(8)	0
G	$-0.90(5)$	$-\frac{11}{12}$	$-0.71(5)$	-	$-0.63(5)$	-	$-0.59(5)$	-

Table 2.2: Comparison of the numerical estimates (n) for the subset fractal dimensions D_S with the exact predictions (e) where available. Uncertainties of the last decimal(s) for each D_S are given in parenthesis.

Chapter 3

Percolation in Deposition Models

We start this Chapter by reviewing some aspects of the percolation theory that are needed for understanding the work presented in the remainder of the Chapter. Next, a 2D deposition model that introduces an effective repulsive interaction between the deposited particles, is discussed.

3.1 Percolation Theory

The publication of Broadbent and Hammersley [4] year 1957 started the study of percolation theory, a widely studied branch in statistical physics [8]. It has applications in modeling of forest fires, diffusion in disordered media, and oil fields [8], etc. The percolation theory with the emphasis on critical phenomena was developed since the 1970s. What the percolation theory is about, is perhaps most simply described by the following example.

Take a large square lattice. Occupy each lattice site with probability p, independently of its neighbors or any other sites. The occupied sites that are nearest neighbors, or that are connected by a continuous chain of nearest neighbor occupied sites form a cluster. Percolation theory deals with the distribution and properties of clusters thus formed.

If the occupation probability p is small, one ends up with small clusters sparsely spread over the lattice. Now, if p is increased, there will at some specific value of p be a spanning cluster, *i.e.*, a cluster that reaches from one end of the lattice to the other. At this point the system is said to percolate.

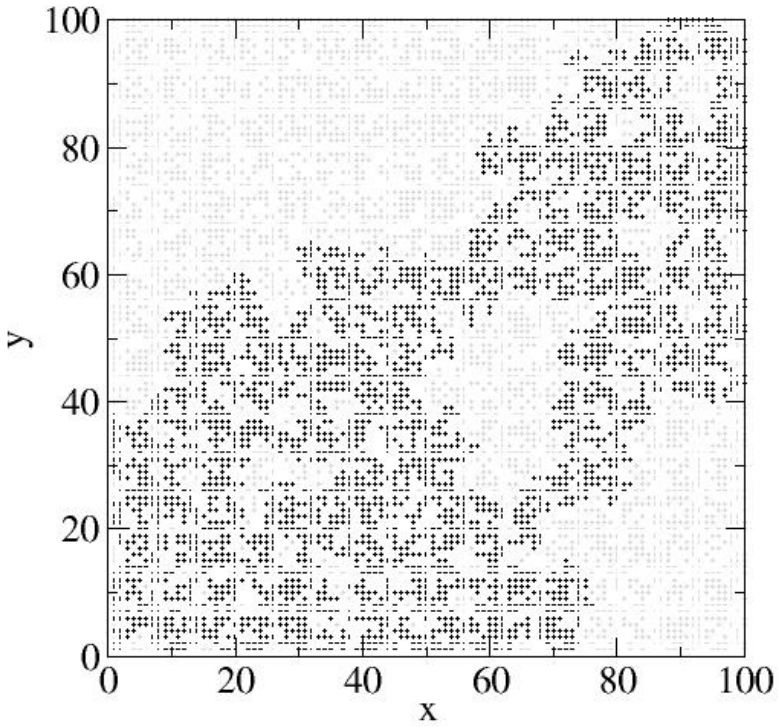

Figure 3.1: A sample configuration of a lattice of size 100×100 at $p_c \approx 0.592746$. The spanning cluster is highlighted with black color, while other clusters are shown in gray.

For an infinitely large lattice, the transition from the state with no spanning cluster to the state with one (or several) takes place at a well defined value of p. This critical value of p is called the *percolation threshold*, p_c. The percolation transition is a geometric transition of second order, in analogy to thermal phase transitions. An example of a square lattice at the percolation threshold is shown in Fig. 3.1.

Let us now consider the lattice at p_c. In a large lattice, there evidently are a lot of clusters of different sizes and shapes. A natural question that arises that what is the distribution of the clusters, that is, what is the probability *per site* to find a cluster of size s, n_s. It is important to note that the

probability of a given site to belong to a cluster of size s is different since it can be any of the s sites occupied by the cluster.

It is plausible to assume that the distribution has a power-law form, since at p_c the mean cluster size is expected to diverge due to the existence of the spanning cluster. The Fisher exponent [98] τ is thus defined through

$$n_s \propto s^{-\tau} \tag{3.1}$$

for large s.

For p larger than p_c, there is a non-zero probability for a site to belong to the infinite cluster. The percolation probability, or the strength of the infinite cluster, P is defined as the probability of an arbitrary site to belong to the infinite cluster. The probability that an arbitrary site belongs to any cluster is therefore equal to the probability p that the site is occupied. Thus

$$P + \sum_s n_s s = p, \tag{3.2}$$

where the sum runs over all finite clusters and excludes the infinite cluster.

Knowing the distribution of clusters, one may want to know what is the average size of a cluster. There is a probability $n_s s$ that an arbitrary site belongs to an s-cluster and a probability $\sum_s n_s s$ that it belongs to any finite cluster. Thus, $w_s = n_s s / \sum_s n_s s$ is the probability that the cluster to which an arbitrary occupied site belongs contains exactly s sites. From this, the average cluster size S can be found as

$$S = \sum w_s s = \sum \frac{s^2 n_s}{\sum w_s}. \tag{3.3}$$

A quantity of general interest is the *correlation length* describing the extent of spatial correlations in the system. In the vicinity of the percolation threshold it is found to diverge as

$$\xi = |p - p_c|^{-\nu}, \tag{3.4}$$

where ν is called *correlation length exponent.*

In analogy to thermal critical phenomena, many of the quantities of interest in percolation theory display power-law divergence (or dependence) near the critical point p_c. One can go through some exactly solvable examples [8] to get a feeling of how some of the exponents can be calculated.

The correlation length exponent ν completely analogous to the correlation length defined in case of thermal phase transitions [99]. The quantity analogous to the mean cluster size in thermal critical phenomena is the susceptibility. S is found to diverge with exponent γ, which in 2D case has the

exact value of $\gamma = 43/18$. The strength of the infinite cluster P, on the other hand, can be related to the magnetization, and the exponent β governing the divergence $P \propto |p - p_c|^\beta$ has the value $\beta = 5/36$ (in 2D). Only two of the exponents are independent; others can be derived from these using the well known scaling relations [8].

Percolation is by no means restricted to a fixed lattice structure. A vast variety of *continuum percolation models* have been studied over the last couple of decades (see e.g. [41, 42, 43]). Instead the occupation probability, one studies the properties of the system as a function of the number density $\eta = N/L^2$, where N is the number of particles and L is the system size. The percolation threshold η_c is defined in analogy to p_c in the lattice models.

The so-called "flocculation model" (FM) [36] was developed to capture some of the features characterizing formation of laboratory paper. In the process, cellulose fibers filtrate from the fiber suspension onto a mesh. Fibers are known to form flocks [33], and this tendency is modeled via an effective attractive interaction described by a parameter p. Fibers are deposited on a two dimensional plane. If a fiber lands on empty space, it is accepted with probability p. In the case it lands on a fiber already present in the network, it is always accepted. For $p = 0$, only a singe cluster is allowed to grow, while for $p = 1$ the resulting fiber network is uniformly random. In the intermediate values of p, interaction causes the network to form of fiber flocks, resulting in non-trivial power-law form of the two-point mass density fluctuation correlation function. The results can be contrasted with those obtained for mass density correlations in real paper sheets [48]. In the work [36], percolation properties of the flocculation model were studied. The percolation threshold $\eta_c(p)$ was found to diverge in the limit $p \to 0$.

One important concept that is often addressed within percolation theory is that of *universality*. For example, all 2D percolation problems with finite-range connectivity are believed to belong in the same *universality class* [8]. It means that the critical exponents describing the behavior of various quantities near p_c are the same independently of the details of the lattice structure as long as the connectivity rule defining the clusters is finite. Also, the exponents are the same for both lattice and continuum percolation.

3.2 Rejection Model

The deposition model studied in the present work, called the "Rejection Model" (RM), was originally introduced by J. Åström [100]. In the RM,

spatially extended objects are sequentially deposited on a 2D plane in continuum according to the following rules:

- The orientation and the spatial coordinates of a deposited object are chosen from a uniformly random distribution.
- If a deposited object lands on empty space, the attempt is always accepted.
- If it lands on another object already on the surface attempt is rejected with a given probability $0 \leq q \leq 1$.

Thus, the parameters that characterize the model are the rejection probability q, the dimensions of the deposited objects, the linear dimension L of the surface, and the number of deposited objects kept N (*i.e.* the number of accepted attempts). One should note that the model generates fractal clusters at the percolation threshold $\eta_c(q)$ with geometric properties identical to those of 2D lattice percolation clusters and Fortuin-Kasteleyn clusters in the $q = 1$ Potts model.

In the limit $q = 0$ the model reduces to the extensively studied case of a uniformly random network [33, 36, 37, 41, 42, 43, 44]. However, for $q > 0$ there is an effective contact repulsion between the particles that tends to prevent overlaps. In particular, for the extreme case of $q = 1$, a strict non-overlap condition is imposed. This is the well-known limit of Random Sequential Absorption (RSA) models [31]. In this case, percolation with connectivity defined through particle overlaps is not possible, and deposition typically terminates to a finite density called the "jamming limit".

Motivation for the model arises in part from deposition of particles such as large charged molecules on surfaces which tend to repel each other. Changing the parameter q allows the tuning of the effective contact repulsion between particles. In the case of equi-charged macromolecules this corresponds to the ratio of the repulsive electrostatic force between the particles and the force binding the particles to the surface. In addition, the RM is complementary to the FM [36, 37, 101]: The parameter space $0 \leq p < 1$ corresponds to effective attractive interactions, while the values of q in the range $0 < q \leq 1$ correspond to repulsive interactions. Both models produce uniformly random networks in the $p = 1$ and $q = 0$ cases.

In the following sections, we study the percolation properties of the networks produced by the RM. Also, spatial correlations of the networks formed are investigated.

3.3 Percolation properties of the model

We first discuss results of numerical simulations of the percolation thresholds $\eta_c(q)$ as a function of q for three different types of objects: needles of length λ, fibers (rectangles) of length λ and width ω ($\lambda > \omega$), and disks of radius r_d. We also summarize the mean-field type arguments that explain the limiting behavior of $\eta_c(q)$ as a function of q in the ends of the parameter range [102].

3.3.1 Numerical Results

The critical densities $\eta_c(q)$ were obtained using the standard Monte Carlo renormalization group (MCRG) method [17, 103], after the curve of spanning probabilities was obtained for each system size L.

Typical configurations generated by the model are shown in Fig. 3.2 for needles of unit length at the percolation threshold for various values of q. The extrapolated values for $\eta_c(q)$ are displayed in Fig. 3.3 (a). The curve displays interesting behavior: First, $\eta_c(q)$ approaches the limit $q \to 0$ approximately linearly. Second, one observes a divergence of $\eta_c(q)$ in the limit $q \to 1$. Our best estimate for $\eta_c(0) = 5.59 \pm 0.05$ agrees well with other numerical studies reported in the literature for the uniformly random case [36, 44]. In addition to the numerical estimates, $\eta_c(0)$ can be approximately determined by using the excluded volume arguments of Ref. [43], where $\eta_c(0)\langle A\rangle = const. \approx 3.57$, and the excluded volume $\langle A\rangle = 0.637$ [43], which gives $\eta_c(0) \approx 5.61$.

(a) (b) (c)

Figure 3.2: Snapshot of networks of needles of length $\lambda = 1$ close to the percolation threshold in a system with $L = 20$, for (a) $q = 0.9$, (b) $q = 0.99$, and (c) $q = 0.999$.

In the case of fibers, we have used objects with an aspect ratio of $\lambda/\omega = 4/1$ as in [36]. In this case, there is no divergence of $\eta_c(q)$ in the limit $q \to 1$,

which in fact is predictable due to the finite are of fibers. We estimate $\eta_c(0) = 2.74 \pm 0.03$, which agrees well with the value reported by Provatas *et al.* [36].

For disks we use the reduced number density $\eta = Nr_d^2/L^2$ as the dimensionless measure for percolation threshold. Our estimate for $\eta_c(0) = 0.36 \pm 0.01$ is in line with other numerical studies reported in the literature [36, 103]. Again, as in the case of fibers, the percolation threshold shows no divergence in the $q \to 1$ limit. The reasons for this will be discussed in the next Section 3.3.2 The critical concentrations for all the geometries of the deposited particles considered here are summarized in Table 3.1.

q / $\eta_c(q)$	Needles	Fibers	Disks
0.0	5.59 ± 0.05	2.74 ± 0.03	.360 ± 0.01
0.2	5.76 ± 0.01	2.75 ± 0.03	.361 ± 0.01
0.4	5.75 ± 0.04	2.77 ± 0.04	.361 ± 0.01
0.6	5.89 ± 0.03	2.77 ± 0.02	.360 ± 0.01
0.8	6.21 ± 0.06	2.83 ± 0.04	.363 ± 0.01
0.9	6.62 ± 0.09	2.87 ± 0.03	.364 ± 0.01
0.95	7.11 ± 0.09		
0.99	9.04 ± 0.03	3.13 ± 0.05	.369 ± 0.01
0.999	15.83± 0.08	3.20 ± 0.03	

Table 3.1: Percolation thresholds $\eta_c(q)$ as a function of q for needles, fibers and disks.

3.3.2 Analytic Theory for Percolation Thresholds

We can qualitatively understand the behavior of the percolation thresholds for the two limits where $q \to 0$ and $q \to 1$ by using mean-field type of arguments, similar to Ref. [36].

Let us start with the small q limit, $q \to 0$. Considering the probability that an object sticks onto any other object in a uniformly random network, and calculating the probability for the N^{th} particle to stick on the plane but not on any of the $N-1$ previously accepted particles, we obtain a lower bound [102] for the critical density near $q = 0$, as

$$\eta_c(q) \;\geq\; Aq + B, \tag{3.5}$$

where A and B are constants [102]. Therefore, we can conclude that $\eta_{c,L}(q)$ increases linearly with q. This is in agreement with our numerical data for the percolation thresholds as can be seen in Fig. 3.3 (b). Our numerical estimate for the constant is $A \approx 0.44$, while the theoretical prediction for the lower bound gives $A = 0.16$ [102].

The divergence of the percolation threshold for needles is to be expected since they have no area associated with them. Because of this they can be packed arbitrarily close to each other. Thus at the final stages of the deposition process at q close to one, the structure of the network is such that there are clumps of needles that are aligned in the same direction. These clumps are then connected to others by the rare needles that are accepted to intersect.

Combining the result of Vigill and Ziff [104], that the number of accepted attempts scales with the number of adsorption attemps with a power $x \approx 0.32$, with an approximation of the number of attempts needed to have one deposited needle accepted in the $q \to 1$ limit [102], we obtain that

$$\eta_c(q) \propto \frac{1}{(1-q)^x}. \tag{3.6}$$

This result is in reasonably good agreement with our numerical data that gives $x = 0.20 \pm 0.05$ (see Fig. 3.3), although, again, it should be noted that our estimate is a lower bound for the true behavior. Also, one would need more data points and better statistics in the $q \to 1$ limit for a better estimate of the exponent x.

In case of objects that have a finite area associated with them, such as disks and fibers, there is no divergence of $\eta_c(q)$. This is due to the finite *jamming limit* η_j in the RSA model [31], where the deposition process terminates since objects are not allowed to overlap. When the number of objects deposited exceeds this limit, the non-overlap condition is violated, and thus there will eventually be spanning in the system. In fact, an upper bound for the percolation threshold for objects of finite area can be estimated as $\eta_c(q) \leq \eta_c(0)+\eta_j$ for all q.

3.4 Cluster Distributions

Cluster distributions were calculated from simulations by taking averages over 1000 realizations for systems with linear sizes $L = 10, 20, 30, 40, 50, 60$

and 80 for various values of the rejection probability q. The clusters were averaged in bins of algebraically increasing sizes.

Numerical estimates for the cluster number exponent τ showed clear size dependence. Our final estimates are based on extrapolation from the finite size scaling of the form $\tau(L) \propto L^{-x}$ with $x \approx 0.25$. Our estimate from extrapolation of $\lim_{L\to\infty} \tau(L)$ yields $\tau \approx 2.0 \pm 0.1$, which is in good agreement with the exact value $\tau \approx 2.05$ in spite of the fact that the system sizes used in the extrapolation are relatively small, and the uncertainty of the percolation threshold.

In Fig. 3.3 (b) we show how n_s varies with q with a relatively small system size ($L = 20$). We note that the algebraically decaying part has roughly the same exponent $\tau \approx 1.7$ independent of q as it should have because of universality. However, for $q \to 1$, the number of small $s \approx 1$ as well as large clusters increases (which is seen clearly in the $q = 0.999$ case). This causes the scaling regime to shrink, so that precise extrapolation of the scaling exponent with the above-mentioned finite-size scaling form becomes difficult.

3.5 Spatial Correlation Functions

3.5.1 Pair Distribution Function

Consider the distribution of centers of mass of needles of unit length. The pair distribution function $\Omega(r)$ is defined through

$$\Omega(r)dr = \Big\langle \frac{\#\text{ of pairs of centers in a shell } (r,\ r+dr)}{\text{total }\#\text{ of pairs of centers in system}} \Big\rangle, \tag{3.7}$$

where the averaging is over all configurations. In Ref. [102] and references therein, it is shown that this can be written in the form

$$\Omega(r)dr = \frac{2}{N(N-1)} \int_A d^2x_0 G_{CM}(r_0, r) \Delta A(x_0 + x), \tag{3.8}$$

where

$$G_{CM}(r_0, r) \equiv \langle \eta_{CM}(\vec{x}_0) \eta_{CM}(\vec{x}_0 + \vec{x}) \rangle. \tag{3.9}$$

Here $\Delta A(\vec{x}_0)$ is the area element around $\vec{x_0}$ and η_{CM} is the ratio $\eta_{CM} = \lim_{\Delta A\to 0}(\Delta N_{CM}/\Delta A)$. The brackets denote configuration averaging. In Ref. [36], it is shown that for a uniformly random set of points with translational invariance this expression equals the exact pair distribution function

Ω_a for a uniformly random network as previously derived by Ghosh [33, 105] as

$$\Omega_a(r,L) = \begin{cases} (4r/L^4)[\pi L^2/2 - 2rL + r^2/2] \ , & \text{for } 0 \le r \le L; \\ (4r/L^4)[L^2\,(\arcsin(L/r) - \arccos(L/r)) & \\ +2L\sqrt{r^2 - L^2} - \frac{1}{2}(r^2 + 2L^2)] \ , & \text{for } L \le r \le \sqrt{2}L \ . \end{cases} \tag{3.10}$$

In Fig. 3.4 we show this function together with our numerical evaluation of the pair distribution function of Eq. (3.7) for various values of q. The remarkable result is that within the numerical errors, there is no dependence on q. This can be explained as follows. For $q > 0$, objects are rejected during the deposition process, but the center-of-mass coordinates of the objects that will stay in the final configuration are still taken from a uniformly random distribution. Since needles have no width associated with them and they can be packed arbitrarily close to each other, the distribution of pairs of centers of masses remains constant in q. We note that this result is in marked contrast to the FM, where a double-peak type of structure in Ω develops when clustering of fibers is enhanced in the limit $p \to 0$ [36].

The behavior of the pair distribution function must depend on q for objects with a finite area associated with them. To illustrate this, we consider here the case of disks of radius r_d. In the RSA limit ($q = 1$), all objects are restricted not to be closer than twice the disk radius r_d. Thus, we can write the RSA approximation Ω_f in this limit as

$$\Omega_f(r) = C\theta(r - r_c)\Omega_a(r), \tag{3.11}$$

where $\theta(r)$ is the step function, and C a normalization constant. In Fig. 7(b) we show results for numerical data for $\Omega(r)$, with $q = 0.9,\ 0.99,\ 0.999$ and 0.9999, and also the function $\Omega_f(r)$. In the limit of $q \to 1$, a cut-off in $\Omega(r)$ develops at $r_c = 2r_d$ corresponding to the non-overlap condition. Following this, there is a sharp peak at $\Omega(r)$ just beyond r_c, where the disks are packed very closely together. We note that the approximation of Eq. (3.11) is unable to reproduce this peak.

3.5.2 The Two Point Mass Density Correlation Function

The two-point mass density fluctuation correlation function is defined as

$$G(\vec{x}) \equiv \langle [m(\vec{x}') - \langle m \rangle][m(\vec{x}' + \vec{x}) - \langle m \rangle] \rangle, \tag{3.12}$$

where $m(\vec{x})$ is the mass density at $\vec{x}$, and $\langle m \rangle$ is the average mass density. This correlation function is a measure of the mass distribution in the network, and the properties of $G(r)$ reflect, e.g., the complex processes occurring during paper-making [48].

We calculated $G(r)$ numerically by discretizing fibers on lattice points. The lattice model was solved with periodic boundary conditions and with the aspect ratio $\omega/\lambda/L = 2/20/150$, which is quite close to the needle limit. The lattice size was checked to be large enough so that finite size effects do not affect the correlation function in the range of interest.

In Fig. 3.5 (a) we show a series of the functions for $q = 0.999$. As N increases towards $N_c \approx 200$, there is an increasing anticorrelation in $G(r)$ just beyond the fiber width $\omega = 2$. This reflects the effective repulsion and local alignment of anisotropic particles present in the model. Moreover, we find that $G(r)$ can be approximated by

$$G(r) \propto r^{-\alpha(N,q)}, \text{ for } 0 < r < \Lambda(N,q), \tag{3.13}$$

where Λ is an effective cutoff for the power law form. The cutoff here is of the order of $\Lambda \approx \lambda/2$ for all values of N [33, 36]. When q is close to unity, $\alpha(N,q)$ goes through a maximum as N increases. Moreover, Λ attains a minimum where α is maximum (see Fig. 3.5 (b)). This is again in contrast to the case of the FM, where the range of the approximate power law form was found to have a maximum close to the threshold, when clustering was enhanced [36]. We note that for $N >> N_c$, the mass density of the networks again approaches the uniform distribution for any $q < 1$ [36].

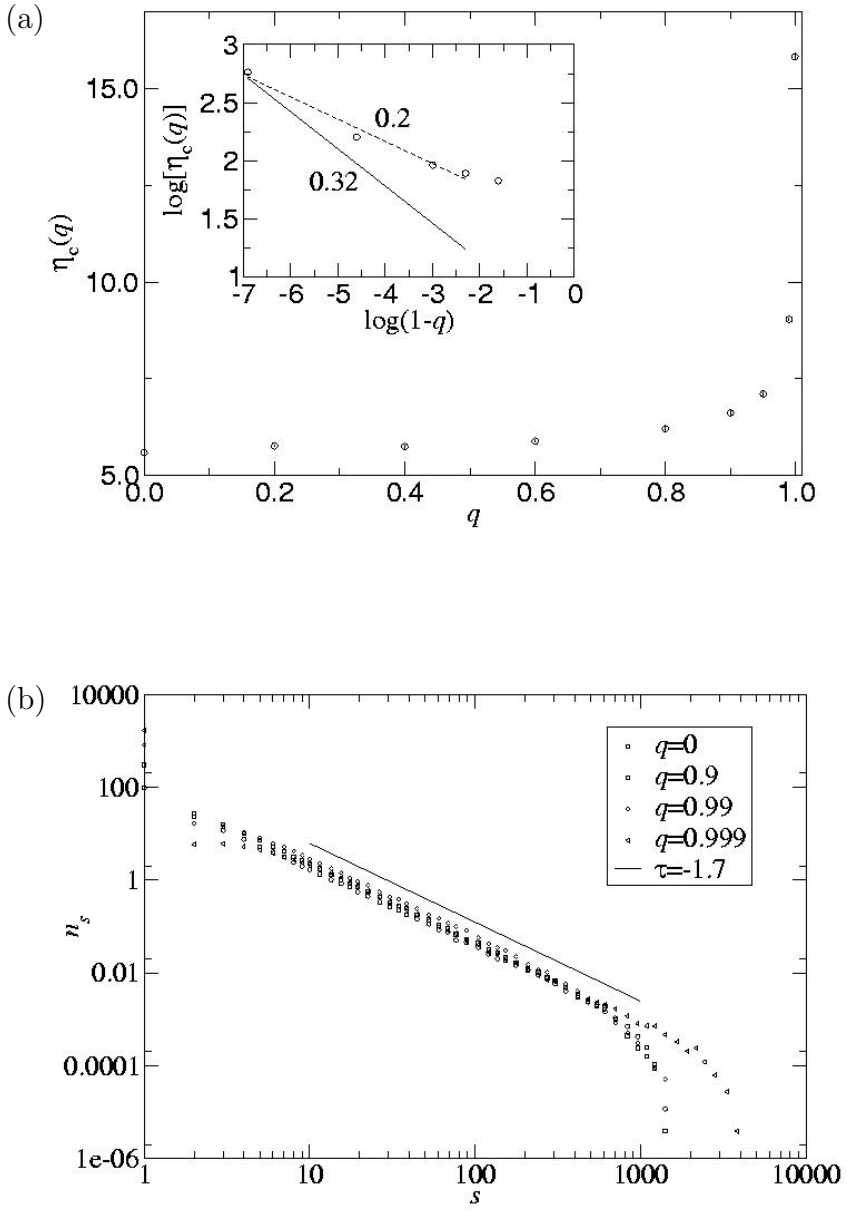

Figure 3.3: (a) The percolation threshold $\eta_c(q)$ vs. q for a network of needles of length $\lambda = 1$. Inset shows the behavior near $q = 1$. (b) Cluster distributions for the needles with various values of the rejection probability q from simulations with $L = 20$.

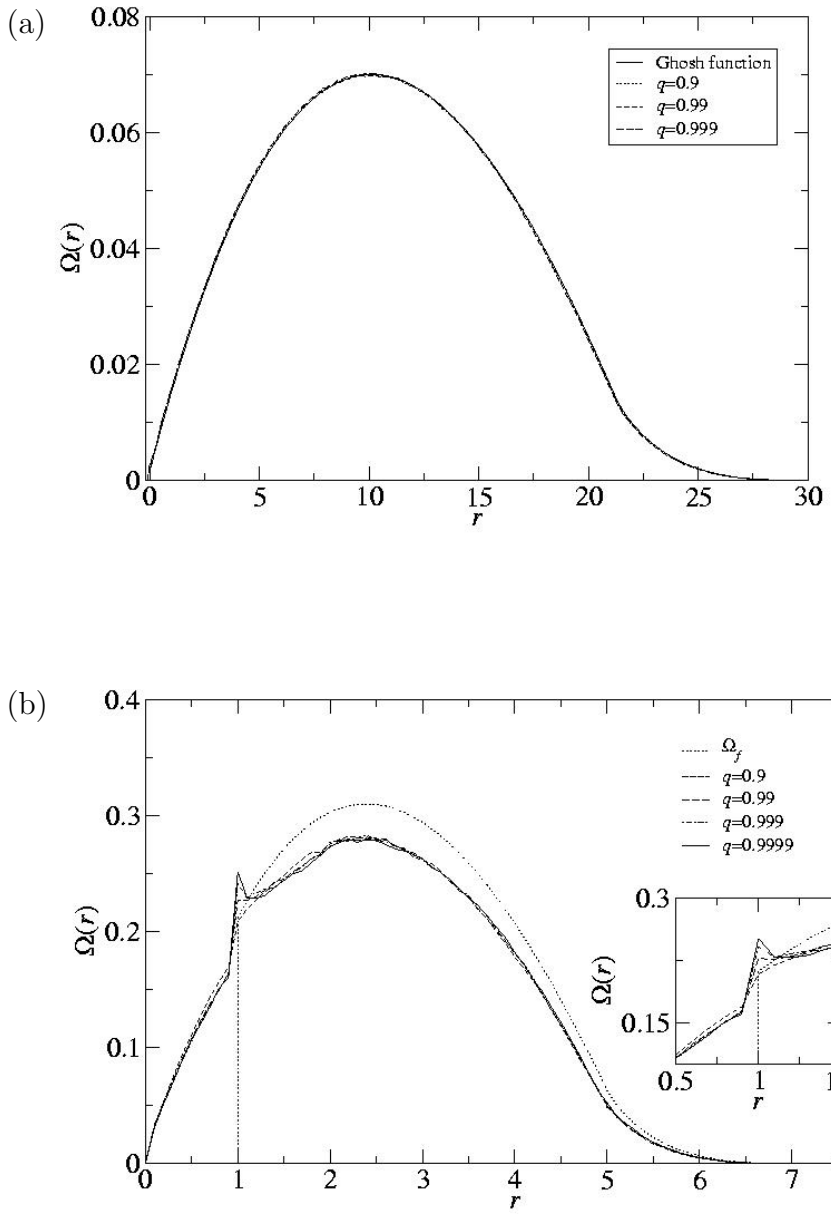

Figure 3.4: Pair distribution functions for (a) needles of length $\lambda = 1$, and (b) disks of radius $r_d = 1/2$. Inset shows a blowup of the pair distribution function at $r_c = 1$ (see text for details).

(a)

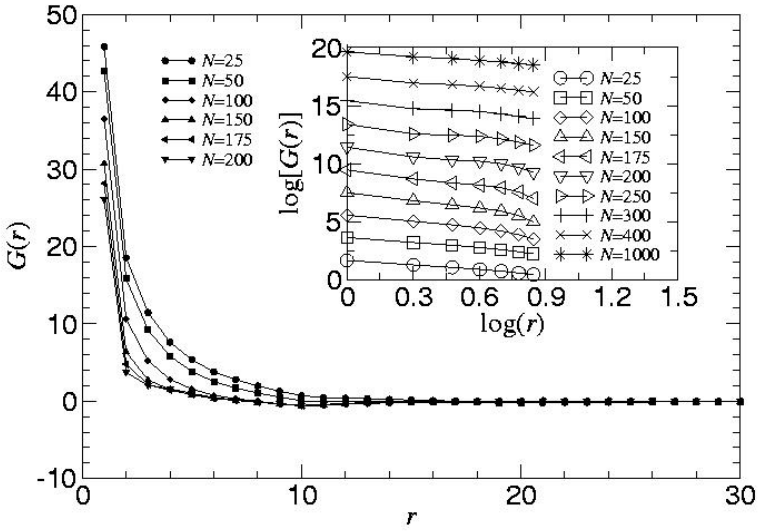

(b)

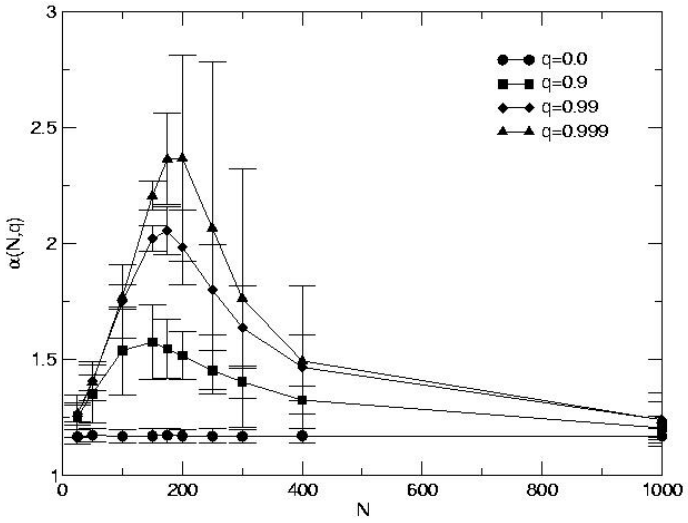

Figure 3.5: (a) The density correlation function $G(r)$ for a discrete approximation of fibres ($\lambda/\omega = 20/2$) vs. N for $q = 0.999$. The inset shows the initial power law type of decay of $G(r)$ for short distances $r < \lambda/2$. (b) The effective exponents of $G(r)$ for various values of q.

Chapter 4

Kinetic Roughening and Interface Dynamics in Fractals

In this Chapter, we consider the dynamics and kinetic roughening of driven interfaces in three classes of lattice fractal growth models, namely the invasion percolation (IP) model [8], diffusion limited aggregation (DLA) model [5] and ballistic deposition (BD) model [106]. We show that the models exhibit rich surface scaling behavior that cannot be explained by standard theories of growth models. In particular, we derive the local scaling exponents of various q^{th} order correlation functions and show that the fractal growth models exhibit intrinsic anomalous scaling [107] and multiscaling. We compare the exact predictions with the results of numerical simulation of the models.

4.1 Scaling properties of single-valued interfaces

For any interface propagating in a random medium, we define a set of single-valued local interface heights $\{h(x_i,t)\}_{i=1}^{L}$ at x_i by the highest occupied lattice site from the reference plane $h=0$ [69]. This corresponds to a solid-on-solid (SOS) description of the interface which excludes any overhangs belonging to the perimeter of a fractal cluster.

A rough surface may be characterized by the fluctuations of the height around its mean value. Thus, the basic quantity to look at is the *global* width

$$w(t,L) \equiv \langle \overline{[h(x,t)-\overline{h}(t)]^2} \rangle^{1/2}, \tag{4.1}$$

where the overbar denotes spatial averaging over x in a system of size L and angular brackets denote configuration (noise) averaging.

For self-affine interfaces, the global widths typically satisfy the Family-Viscek (FV) scaling ansatz [64]

$$w(t, L) = t^{\beta} f(L/\xi(t)) \tag{4.2}$$

where the scaling function $f(u)$ satisfies

$$f(u) \sim \begin{cases} u^{\chi}, & \text{for } u \ll 1; \\ const., & \text{for } u \gg 1. \end{cases} \tag{4.3}$$

In these equations χ is the roughness exponent and characterizes the stationary regime, in which the correlation length $\xi(t) \sim t^{1/z}$, where z is the dynamic exponent, has reached $\xi \approx L$. The ratio $\beta = \chi/z$ is called the growth exponent and characterizes the evolution of temporal correlations of the surface [9].

In many cases of interest, there is a description of kinetic roughening processes in terms of a stochastic equation of motion for the (single-valued) height function $h(\vec{x}, t)$. The best known example is the Kardar-Parisi-Zhang (KPZ) equation [54]

$$\frac{\partial h(\vec{x}, t)}{\partial t} = \nu \nabla^2 h(\vec{x}, t) + \frac{\lambda}{2} |\nabla h(\vec{x}, t)|^2 + \eta, \tag{4.4}$$

where η is a noise term. For strongly driven interfaces, the noise term is usually uncorrelated in space and time, but in some cases it may also depend on h in which case the noise is quenched. The scaling exponents of the KPZ equation are $\chi = 1/2$ and $\beta = 1/3$ [9] for 1D interfaces.

Many growth phenomena in nature are well described by the KPZ equation. However, some experiments have revealed different scaling. For example, Rubio *et. al.* [25] measured a roughness exponent $\chi \approx 0.73$ and Hovárth *et. al.* [26] $\chi \approx 0.81$ in fluid invasion experiments, while Vicsek *et. al* [27] measured $\chi \approx 0.78$ in context of growth of bacterial colonies. Similar values for the scaling exponents can be obtained from variants of the KPZ equation where the noise amplitude is power-law distributed [58, 60, 61, 62].

Some growth models exhibit different scaling of global and *local* interface fluctuations. This can be quantified by defining a local width of the interface $w(t, \ell)$ as

$$w(t, \ell) \equiv \langle \langle [h(x, t) - \langle h(t) \rangle_{\ell}]^2 \rangle_{\ell} \rangle^{1/2}, \tag{4.5}$$

where $\langle \cdots \rangle_\ell$ denotes an average over x in windows of spatial size ℓ. When local and global roughening processes differ, the surface is said to exhibit *anomalous scaling* [107]. In this case, the scaling of the local width is of the form of Eq. (4.2), $w(t,\ell) \sim t^\beta f_A(\ell/\xi(t))$ with the anomalous scaling function $f_A(u)$ satisfying

$$f_A(u) \sim \begin{cases} u^{\chi_{\rm loc}}, & \text{for } u \ll 1; \\ const., & \text{for } u \gg 1, \end{cases} \tag{4.6}$$

where the new independent exponent $\chi_{\rm loc}$ is called the local roughness exponent. Anomalous scaling has been found to occur in many growth models [108, 109, 110] as well as observed in experiments [28, 29, 111]. Also variants of the KPZ equation where the noise is spatially correlated [55, 56, 57] have been shown to exhibit anomalous scaling. Anomalous scaling thus implies that there is one more independent exponent $\chi_{\rm loc}$ describing local roughness of the interface.

It is not always possible to write an equation of motion such as Eq. (4.4) for the local height variable $h(x,t)$. Examples include the directed percolation depinning model (DPD) [9, 67, 68], which is the pinned limit of the KPZ equation with quenched noise. For DPD, the interface roughness can be related to the geometric properties of the underlying directed percolation cluster, namely, the roughness exponents the ratio of the perpendicular and the lateral correlation length exponents [9]. Also, there exist models in which the natural interface is multi-valued. Thus, if one defines a single valued height profile $h(x,t)$ the overhangs play a significant role in the statistics of $h(x,t)$. Example of such models include the lattice "forest fire" models [69, 70] and the diffusion limited aggregation model (DLA) [5] the so called multiparticle biased diffusion limited aggregation (MBDLA) [72, 112]. For all such cases there exists no theoretical explanation of the roughening properties of the interfaces at present. In the work reported in Publications IV and V this aspect is clarified. In particular, we show that from the statistics of the nearest neighbor single-valued height differences one can deduce the nature of the roughening process.

To examine the local properties of the interfaces, we define the $q^{\rm th}$ order height difference correlation function as

$$G_q(x,t) = \langle \overline{|h(x_0,t) - h(x_0+x,t)|^q} \rangle^{1/q}, \tag{4.7}$$

with G_q satisfying the anomalous scaling relation [69, 113]

$$G_q(x,t) = \xi^{\alpha_q} x^{\chi_q} f_q(x/\xi). \tag{4.8}$$

Here, the scaling function $f_q(u \to 0) = const.$ and $f_q(u \to \infty) \propto u^{-\chi_q}$ [69]. The exponents α_q define the so-called anomaly exponents, and χ_q's define local roughness exponents, with $\chi_{\rm loc} = \chi_2$ [110, 113].

A quantity measuring the temporal development of the local roughness of the interfaces is the average nearest neighbor height difference function $\sigma_q(t)$, defined by [108]

$$\sigma_q(t) = \langle \overline{|h(x_{i+1}, t) - h(x_i, t)|^q} \rangle^{1/q}, \tag{4.9}$$

which at early times follows the scaling relation

$$\sigma_q \sim \xi^{\alpha_q} \sim t^{\alpha_q/z} \sim t^{\beta_q}, \tag{4.10}$$

where β_q's are the local growth exponents. At late times, σ_q's saturate to system size dependent values.

One can also define the time-dependent $q^{\rm th}$ order height-height fluctuation correlation function [114]

$$C_q(t) = \langle \overline{[\delta h(x, t_0) - \delta h(x, t_0 + t)]^q} \rangle^{1/q}, \tag{4.11}$$

where $\delta h \equiv h - \overline{h}$ is the deviation from the average height. In the saturated regime, one expects C_q to scale as $C_q \sim t^{\bar{\beta} q}$ at early times, and to saturate to a system size dependent value at large times. If the $q^{\rm th}$ order correlation functions of Eqs. (4.7), (4.9) and (4.11) exhibit q dependent scaling exponents, the surfaces are said to be multifractal [115], or to exhibit multiscaling.

Recently, Ramasco *et al.* [107] proposed a generalized scaling theory. The corresponding scaling form incorporates all the different forms known thus far that dynamical scaling can take and predicts the existence of a new class of growth models with novel anomalous scaling properties. Let $\hat{h}(k, t) = L^{-1/2} \sum_x [h(x, t) - \bar{h}(t)] \exp(ikx)$ be the Fourier transform of the height of the surface in a system of size L. The whole scaling picture can be expressed in terms of the scaling of the structure factor

$$S(k, t) = \langle \hat{h}(k, t) \hat{h}(-k, t) \rangle. \tag{4.12}$$

Note that the other quantities such as the global and local width can be obtained from $S(k, t)$ [107]. If the roughening process under consideration shows generic dynamic scaling, that is $\xi(t) \sim t^{1/z}$ for small times and $\xi \sim L$ in the saturated regime [107], then the scaling of the structure factor is given by

$$S(k, t) = k^{-(2\chi+1)} s(kt^{1/z}), \tag{4.13}$$

where the scaling function has the general form

$$s(u) \sim \begin{cases} u^{2(\chi-\chi_s)}, & \text{for } u \gg 1; \\ u^{2\chi-1}, & \text{for } u \ll 1, \end{cases} \tag{4.14}$$

and the exponent χ_s is called the *spectral* roughness exponent. Now, the scaling properties of the interface can be classified according to the values of χ, $\chi_{\rm loc}$, and χ_s as follows [107]:

$$\begin{cases} \text{if } \chi_s < 1 \Rightarrow \chi_{\rm loc} = \chi_s \begin{cases} \chi_s = \chi \Rightarrow \text{Family} - \text{Vicsek}; \\ \chi_s \neq \chi \Rightarrow \text{Intrinsic anomalous}; \end{cases} \\ \text{if } \chi_s > 1 \Rightarrow \chi_{\rm loc} = 1 \begin{cases} \chi_s = \chi \Rightarrow \text{Superrough}; \\ \chi_s \neq \chi \Rightarrow \text{New class}. \end{cases} \end{cases} \tag{4.15}$$

The difference between superroughening and intrinsic anomalous roughening has already been noted by López *et al.* [113]. All other classes can be distinguished from the difference between local and global scaling of the width, but the new scaling class is distinguishable from the structure factor only [107]. It will be shown in Sect. 4.2 that here the growing interfaces in the fractal models studied are intrinsically anomalous, and they exhibit *multiscaling* in terms of the local exponents.

4.2 Exact results for scaling exponents

4.2.1 Local slope distributions

For the case of the KPZ equation without quenched randomness, it is well known [9] that the steady-state distribution of local slopes of the height variables ∇h in 1D is Gaussian, $P(\nabla h) \sim \exp[-(\nabla h)^2]$ (one should note that $P(\nabla h)$ for interface equations such as the KPZ equation (4.4) may depend on the parameters entering the equation). However, in systems where quenched noise is present, the underlying probability distributions are typically of Lévy type, that is, they have an algebraic decay form [116].

In Publication IV we consider the probability distribution function $P(\Delta h)$ for local nearest-neighbor (NN) slopes $\Delta h \equiv |h(x_{i+1}) - h(x_i)|$ for an isotropic IP model. Through exact scaling arguments we show that it has a Lévy distribution of the form

$$P(\Delta h) \sim (\Delta h)^{-\alpha}, \tag{4.16}$$

where $\alpha = 2$. This result holds also for the 2D nearest neighbor lattice forest fire model at the percolation threshold [69]. Let us now consider such

distributions with $\alpha > 1$ [116]. In Publications IV and V, we show how Eq. (4.16) can be used to derive expressions for the local scaling exponents. The local growth exponents governing the early time scaling of the functions $\sigma_q(t)$ are given by

$$\beta_q = (1 + \frac{1-\alpha}{q})\beta. \tag{4.17}$$

Furthermore, we show in Publications IV and V that the local roughness exponent can be obtained by combining the scaling of $\sigma_q(t)$ and $G_q(x,t)$ yielding

$$\chi_q = 1/q. \tag{4.18}$$

In addition, we obtain the prediction for the *global* roughness exponent as

$$\chi = \frac{1}{\alpha - 1}. \tag{4.19}$$

In Publication V we present numerical evidence supporting our conclusion that the local roughness exponents χ_q indeed are independent of the decay exponent α.

These results show that both the local and global roughness exponents are uniquely determined by the statistics of the NN slopes, which is the fundamental quantity here. It is also evident from Eq. (4.18) that multiscaling [115] and intrinsic anomalous roughening occur for $\alpha > 1$, but that the interfaces are never superrough since $\chi_{\mathrm{loc}} = \chi_2 = 1/2$ [107]. Our results can be compared with the recent scaling approach to calculate the scaling exponents by López [117].

4.2.2 Generalized scaling

To explain the scaling behavior of $C_q(t_0, t)$ we define a generalized correlation function $\tilde{C}_q(x, t_0, t)$ as

$$\tilde{C}_q(x, t_0, t) \equiv \langle \overline{|\delta h(x_0, t_0) - \delta h(x_0 + x, t_0 + t)|^q} \rangle^{1/q}. \tag{4.20}$$

In Publication V, we present the derivation of the exponents $\tilde{\beta}_q$ describing the scaling of the functions $C_q(t)$ using the generalized correlation function of Eq. (4.20) and as a result

$$\tilde{\beta}_q = \beta - \beta_q. \tag{4.21}$$

The scaling of $\tilde{C}_q$ can be generalized even further by including the scaling with the system size L. The scaling ansatz then yields finite size scaling of the correlation function $C_q(t, L)$:

$$C_q(t, L) = L^{\chi} F_q(t/L^z), \tag{4.22}$$

where the new scaling function $F_q(s) \sim s^{\tilde{\beta}_q}$ for $s \ll 1$, in analogy with the FV scaling form. These scaling forms are numerically tested in Section 4.4.2.

4.3 Fractal models

To study the validity of our theory of Chapt. 4.2, we calculate the correlation functions defined in the previous Section in three well-known models. These models are reviewed in this section. All fractal models are grown in 2D rectangular geometry with periodic boundary conditions in lateral direction, starting with an initially occupied bottom row.

4.3.1 Invasion percolation

Invasion percolation models [118] constitute an important and widely studied class of percolation theory. The IP is a dynamic percolation process that describes the displacement of one fluid by another in a porous medium in the limit where capillary forces dominate the viscous forces [8]. A typical invasion percolation cluster is shown in Fig. 4.1(a), and Fig 4.1(b) shows a sequence of corresponding single-valued interfaces. The growth rule of the IP model is to choose, at each time step, the site on the perimeter of the existing cluster the site, which has the smallest capillary number associated with it, and to advance the invading cluster to that site. The site is then removed from the growth sites and new growth sites checked. The process is then iterated.

IP can be divided in two cases: one with trapping (TIP) and the other without it (NTIP). TIP describes a situation in which the defender fluid is incompressible, and thus invasion process terminates in regions fully surrounded by invading fluid. The NTIP model, on the other hand, is consistent with the case where the defending fluid is compressible. An important property of the NTIP model is that it is believed to to be equivalent to ordinary percolation [119], which means that its geometric properties are well known. The details of the implementation of the model can be found in Appendix B.

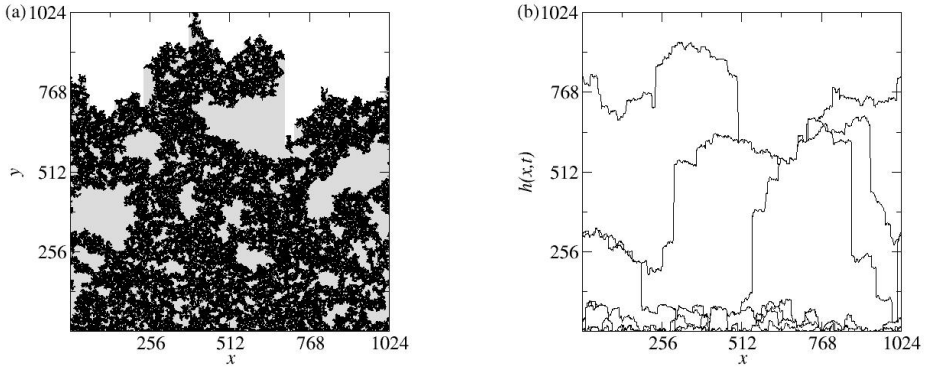

Figure 4.1: Snapshots of a (a) fractal cluster and (b) a series of single-valued interfaces as generated by the NITP model. The shading in (a) indicates how overhangs are cut off to define the interface.

4.3.2 Diffusion limited aggregation

Diffusion limited aggregation is a model of irreversible growth to generate fractal structures as proposed by Witten and Sander [5]. It has been used to study a great variety of processes: dendritic growth, viscous fingers in fluids, dielectric breakdown, electrochemical deposition *etc.* [71]. A typical DLA cluster is shown in Fig. 4.2(a), with single-valued interfaces in (b). At each step, a walker is launched at a randomly chosen position on a line, which is one lattice unit higher than the highest occupied site in the aggregate. The walker then performs random walk until it sticks to the cluster. This process is then repeated until the desired cluster size is reached.

To enable simulations of large systems we have developed an *exact* and efficient method to speed up *discrete* random walk in complicated environments. In Publication VI, it is shown that by this method, one wins a factor of L in the scaling of total CPU time per particle $t_{\mathrm{tot}}(L)$ with system size L. In Appendix C, we show some details of the method and some aspects of efficient implementation of the method.

4.3.3 Ballistic deposition

Ballistic deposition was introduced as a model of colloidal aggregates, and early studies concentrated on the properties of the porous aggregate produced

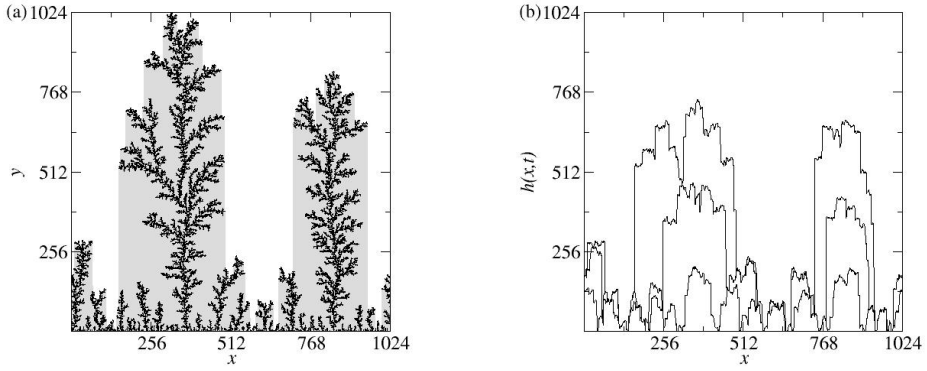

Figure 4.2: Snapshots of a (a) fractal cluster and (b) a series of single-valued interfaces as generated by the DLA model. The shading in (a) indicates how overhangs are cut off to define the interface.

by the model (see Ref. [9] and references therein). We study a modified version of the original model, introduced by Karunasiri *et al.* [106]. In the model, a random position is chosen for the particle. Then the particle is launched at an angle θ, which chosen from a uniform distribution $P(\theta)$, with $-\pi < \theta < \pi$. Particle follows a straight (off-lattice) trajectory until it reaches a nearest neighbor site of the aggregate, where it sticks.

This model is known to exhibit instable growth known as the shadow instability [106]. In the case of low-temperature sputter deposition of amorphous and polycrystalline thin films, the shadow instability is known to play a significant role in determining the surface morphology [120]. An example of a cluster produced by the modified BD model is shown in Fig. 4.3(a), and series of single-valued interfaces in (b). We used bit-packing techniques in our simulations [121].

4.4 Results

In this section, we present our numerical results from computer simulations of the three fractal models. We will first demonstrate, that for all the three models considered here a Lévy type of slope distribution function follows, and then discuss direct numerical findings of the scaling exponents.

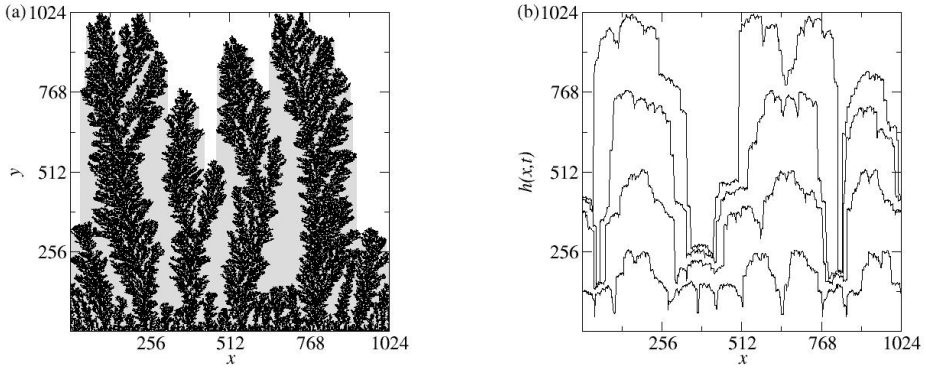

Figure 4.3: Snapshots of a (a) fractal cluster and (b) a series of single-valued interfaces as generated by the BD model. The shading in (a) indicates how overhangs are cut off to define the interface.

4.4.1 Local slope distributions and roughness exponents

Invasion percolation

For the case of an isotropic percolation cluster, we have in Publication IV shown through an analytic argument that the exponent α is given exactly by $\alpha = (\tau - 1)D = 2$, where $\tau = 187/91$ and $D = 91/48$ are the cluster size probability exponent and the cluster's fractal dimension, respectively. In fact, a more general relation $(\tau - 1)D = d$, where d is the spatial dimension, can easily be derived from the hyperscaling relation of percolation theory [8] and the equations connecting the scaling exponents [8]. Numerical results for the exponents also support the finding (see the list of critical exponents in [8]).

Using Eq. (4.19) this leads to the prediction that $\chi = 1$, which is also expected due to the spatial isotropy of the cluster [69]. In Fig. 4.4 (a) we show $P(\Delta h)$ as determined numerically for the NITP model, and we indeed find that $\alpha = 2.00 \pm 0.05$. For the global roughness exponent we find using Eq. (4.3) that $\chi = 0.99 \pm 0.02$. The numerical estimates for the local scaling exponents are in excellent agreement with the prediction $\chi_q = 1/q$. The scaling exponents are summarized in Table 4.1. We also verified the anomalous scaling form of Eq. (4.8) as shown in Fig. 4.4 (b).

In the inset of Fig. 4.4 (a) we also show results for the TIP model, for which $\alpha = 1.9 \pm 0.1$. Thus, within our numerical accuracy the two models have the same α, and thus identical roughness exponents. This is not a trivial result since numerical estimates for the TIP model give $D \approx 1.82$ [118], a value somewhat lower than $91/48 \approx 1.90$.

Diffusion Limited Aggregation

For the DLA model the distribution function displays more complicated behavior than in the IP case as can be seen in Fig. 4.5 (a). An interesting feature in $P(\Delta h)$ is that there seem to be roughly three regimes in it. For small values of Δh, the effective α has a value of close to 2.0, after which it levels off to about $\alpha = 1.6 \pm 0.1$. According to our predictions changing α should change χ, and we have verified this by directly computing χ from the global width for systems of different sizes. The results are in the inset of Fig. 4.5 (a). Two distinct scaling regimes are visible, with $\chi = 1.05 \pm 0.03$ and $\chi = 1.21 \pm 0.04$ for the set of smaller and larger system sizes, respectively. We also measured the global roughness exponent from the structure factor $S(k,t)$ to be $\chi = 1.35 \pm 0.10$, in agreement with the second regime. Again, the local χ_q's are in excellent agreement with theory, as can be seen in Table 4.2. Finally, for very large values of Δh there is a distinct bump in $P(\Delta h)$. We shall discuss the reasons and implications of this non-algebraic tail of the distribution Chapt. 4.4.2.

Ballistic Deposition

Conclusions similar to that of the DLA case apply to the BD model as well. In Fig. 4.5 (b) we show three slope distribution functions, for systems of sizes $L = 128$, 1024, and 4096. In these three cases, the different regimes are clearly visible. For the smallest system, α is very close to 2.0, while for the larger systems the effective values of α for larger slopes are reduced to about 1.7 ± 0.1 and 1.6 ± 0.1, respectively. The inset shows χ as measured directly from the global width, showing how the effective χ tends to increase with system size corresponding to the decreasing slope distribution exponent. Again, a bump is visible in $P(\Delta h)$ for the largest slopes. In Ref. [122] $\chi \approx 1$ was measured for the BD model, corresponding to smaller system sizes as in the inset. The local roughness exponents are summarized in Table 4.3.

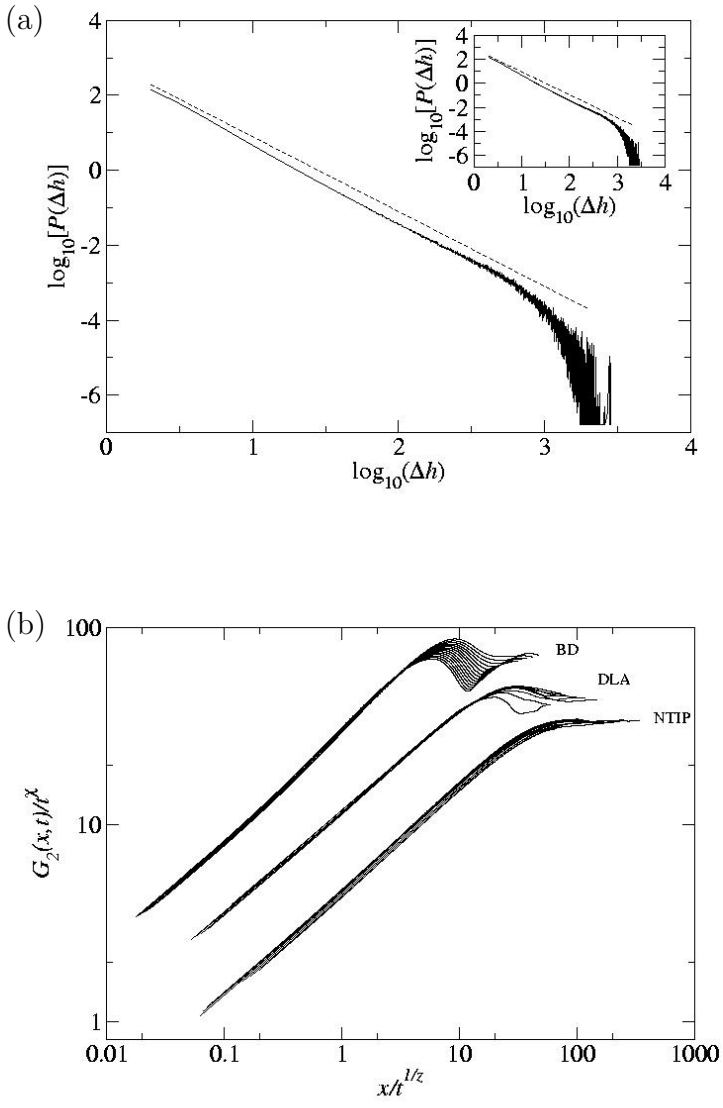

Figure 4.4: (a) The distribution function $P(\Delta h)$ for the NTIP model. Inset shows $P(\Delta h)$ for the TIP model. Dashed lines show the slope $\alpha = 2$. The system size for both cases is 1024. (b) Scaling of the correlation functions $G_2(x,t)$ for the three models. The groups of curves for different models have been shifted for clarity. The exponents used in the data collapse are $\chi = 1, 1.3,$ and 1.25, and $z = 1, 1,$ and 1.25 for the NTIP, DLA, and BD models, respectively.

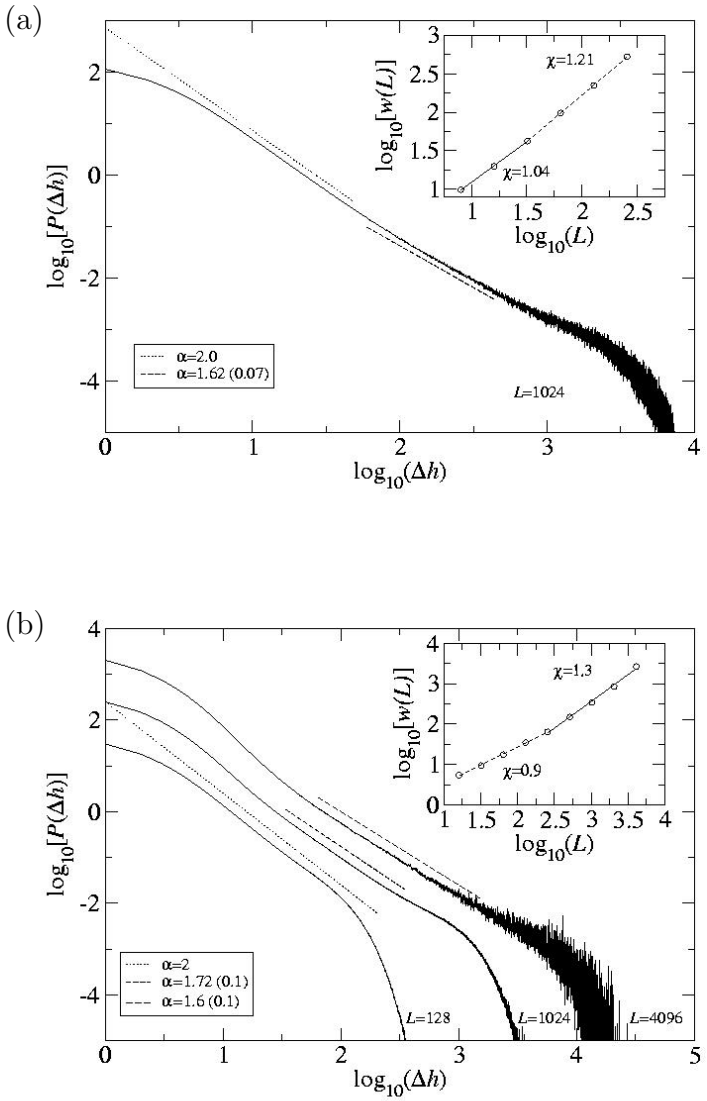

Figure 4.5: (a) The distribution function $P(\Delta h)$ for the DLA model for $L = 1024$. Inset shows the scaling of $w(L)$ with the system size L, with a clear crossover around $L = 16$. See text for details. (b) A series of distribution functions $P(\Delta h)$ for the BD model for different system sizes. Changes in the effective slopes are evident (see text for details). Inset shows the scaling of $w(L)$ with the system size L, with a crossover around $L = 128$.

4.4.2 Temporal scaling and correlation functions

Invasion Percolation

We have measured β directly from $w(t)$ and find that it grows linearly in time, *i.e.* $\beta = 1.00 \pm 0.03$. This indicates that the dynamic exponent $z = 0.99 \pm 0.05$. This differs from the so-called isotropic percolation depinning [69] case for which $z \approx 1.13$. In particular, this demonstrates how changing the dynamical rules from those of the NITP model to the nearest-neighbor "forest fire" model of Ref. [69] changes the the dynamics even though the geometry of the structures is the same. Our numerical estimates for the scaling exponents of the q^{th} order temporal correlation functions are in excellent agreement with the theory is very good as can be seen in Table 4.1. The numerical estimates for the exponents in the TIP model are indistinguishable from the NTIP case.

To check the validity of the scaling formulas derived in Section 4.2.2, we have numerically evaluated the corresponding scaling functions. Aggreement is found to be good (see Publication V for details). Finally, the finite-size scaling for the functions $C_2(t, L)$ with various system sizes L are shown in Fig. 4.6 (b) for the NTIP model. The inset shows the raw data, and in the main figure we observe very good scaling as predicted by Eq. (4.22).

Diffusion Limited Aggregation

The growth exponent is $\beta = 1.35 \pm 0.02$ as measured directly from $w(t)$, and the dynamic exponent $z = 1.0 \pm 0.1$. Since the local exponents governing the scaling of the temporal q^{th} order correlation functions (4.9) and (4.11) β_q and $\tilde{\beta}_q$ depend explicitly on α, which itself changes with system size (and the magnitude of the NN slopes), it is not possible to uniquely determine the values for these exponents. Despite this problem, relatively good agreement with the exponent relation (4.21) can be obtained when $\alpha \approx 2$ [corresponding to the NN slope distribution of Fig. 4.5 (a)] as can be seen in Table 4.2 where we summarize the exponents from these fits.

Ballistic Deposition

Our estimate for the growth exponent is $\beta = 1.16 \pm 0.03$, as measured for the largest system of size $L = 131072$ from the global width $w(t)$. For smaller system sizes we measured a somewhat smaller value for the growth exponent

q	β_q	$\tilde{\beta}_q$	χ_q
1	$\mathcal{O}(\log)$	$.95 \pm .04$	$.86 \pm .01$
2	$.51 \pm .05$	$.51 \pm .01$	$.51 \pm .02$
3	$.67 \pm .04$	$.33 \pm .02$	$.34 \pm .02$
4	$.73 \pm .02$	$.24 \pm .01$	$.26 \pm .01$
5	$.75 \pm .03$	$.19 \pm .02$	$.20 \pm .02$
6	$.77 \pm .02$	$.16 \pm .02$	$.17 \pm .02$
	$1 - 1/q$	$1/q$	$1/q$

Table 4.1: The local scaling exponents from numerical simulations of the NTIP model. Analytic predictions are shown in the lower part of the Table.

$\beta \approx 0.95$ is consistent with value measured in Ref. [122]. The estimate for the dynamic exponent is $z = 1.12 \pm 0.07$. As in the DLA case, it's not possible to pin down the values of the local exponents β_q and $\tilde{\beta}_q$. The results of least-squares fitting are in Table 4.3. Again, when we use $\alpha \approx 2.1$ the numerical results are in good agreement with theory.

In the case of DLA and BD, we argued that the function $P(\Delta h)$ has a non-algebraic tail for large when NN slopes become large. This can in fact also be seen from the q^{th} order nearest neighbor height difference correlation function $\sigma_q(t)$. The functions $\sigma_q(t)$ for small t, have the q dependent power law exponents β_q as given by Eq. (4.17). However, for longer times these functions turn parallel as demonstrated in Fig. 4.6 (a) for the BD model with $L = 4096$.

In this regime, the local growth exponents become independent of q. After another crossover time, the usual saturation regime starts. We find within our numerical accuracy that the exponent β' describing the scaling of the functions $\sigma_q(t)$ in the intermediate regime equals the global roughness exponent $\beta' = \beta$ (see Fig. 4.6 (a)). This means that multiscaling vanishes in this regime. We believe that this change is related to the well-known shadowing instability for DLA and BD models [106], which leads into a change in the evolution of the interface morphology at later times. This conclusion is also supported by the fact that in the NITP model, this phenomenon does not occur.

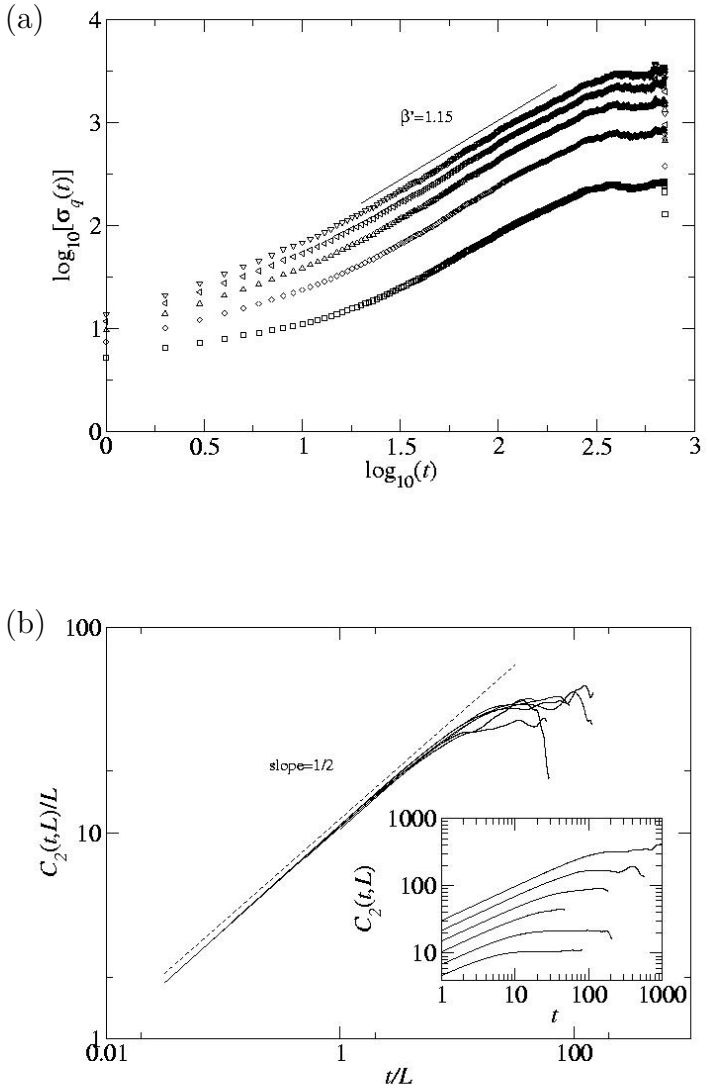

Figure 4.6: (a) The nearest neighbor height difference function $\sigma_q(t)$ for the BD model. After the first crossover time curves turn parallel, and multiscaling in time vanishes (see text for details). From bottom to top, data are for $q = 2, \ldots, 6$. (b) Scaling of the correlation function $C_2(t, L)$ with the system size for the BD model. The range of system sizes is $L = 128, \ldots, 2048$. The correlation functions were evaluated in the saturated regime.

q	β_q	$\tilde{\beta}_q$	χ_q
1	$.27 \pm .02$	$.89 \pm .02$	$.86 \pm .02$
2	$.71 \pm .02$	$.49 \pm .02$	$.52 \pm .02$
3	$.91 \pm .02$	$.32 \pm .02$	$.36 \pm .02$
4	$1.01 \pm .02$	$.24 \pm .02$	$.27 \pm .02$
5	$1.07 \pm .02$	$.19 \pm .02$	$.22 \pm .02$
6	$1.11 \pm .02$	$.15 \pm .02$	$.19 \pm .02$
	$[1 + (1 - \alpha)/q]\beta$	$\beta - \beta_q$	$1/q$

Table 4.2: The local scaling exponents from numerical simulations of the DLA model. The determination of the growth exponents is discussed in the text. Analytic predictions are shown in the lower part of the Table, and they agree quite well with the simulations for $\alpha \approx 2$, $\beta = 1.35$.

q	β_q	$\tilde{\beta}_q$	χ_q
1	$.00 \pm .05$	$.86 \pm .02$	$.97 \pm .02$
2	$.51 \pm .02$	$.50 \pm .02$	$.54 \pm .02$
3	$.66 \pm .02$	$.32 \pm .02$	$.37 \pm .02$
4	$.73 \pm .02$	$.24 \pm .02$	$.28 \pm .02$
5	$.78 \pm .02$	$.19 \pm .02$	$.23 \pm .02$
6	$.81 \pm .02$	$.15 \pm .02$	$.19 \pm .02$
	$[1 + (1 - \alpha)/q]\beta$	$\beta - \beta_q$	$1/q$

Table 4.3: The local scaling exponents from numerical simulations of the BD model. Determination of the growth exponents is discussed in the text. Analytic predictions are shown in the lower part of the Table, and they agree with simulations for $\alpha \approx 2.1$, $\beta = 1.16$.

Chapter 5

Summary and Conclusions

In this work, various aspects of problems concerning fractals have been considered. In the first part, fractal geometry of the Potts clusters at the critical temperature has been examined. The aim was to find numerical evidence on the exactly derived subset fractal dimensions D_S [18, 73, 19, 20] and to give estimates on the dimensions for which exact solution lack. We have given the first numerical estimate of the fractal dimensions D_G describing the scaling of the gates to fjords, which, rather surprisingly are negative [19]. Analysis of numerical data revealed slow and complex approach to the asymptotic behavior. If this is neglected in data analysis, wrong numerical estimates for the dimensions D_S follow. We have derived exact corrections-to-scaling terms using renormalization group and Coulomb gas approaches. Using the correction terms in the fitting procedure, excellent agreement with most of the exact dimensions and data has been found. The present quality and range of data did not allow quantitative confirmation of the exact correction parameters.

In the second part we have presented a study on the so called rejection model. In the model, there is an effective repulsive interaction, described by the rejection probability q, between the deposited objects. The model is complementary to the previously introduced flocculation model [36] where there is an effective attractive interaction between the deposited particles. Furthermore, the model serves as a simple model for the deposition process where equally charged macro-molecules are brought to the surface. In the case where the deposited objects are one dimensional line segments, or needles, the percolation threshold η_c has been found to diverge in the $q \to 1$ limit. In the opposite limit $q \to 0$, for all geometries, η_c has been found to grow linearly with q. For both limits, a mean field theory has been derived to

explain the behavior of η_c. We have also studied the cluster distributions of the networks formed at the percolation threshold and found agreement with the universal power-law decay of the distribution [8]. The networks formed by the deposition process have been shown to exhibit nontrivial correlations. The results can be compared with those obtained in previous studies and experiments [36, 101].

Finally, in the last part of the thesis, we have studied kinetic roughening of driven fronts in fractals. Starting with the isotropic invasion percolation model, we have showed that using results from the percolation theory the form of the probability distribution for the nearest neighbor slopes, $P(\Delta h)$ can be derived. The probability distribution has an algebraically decaying form $P(\Delta h) \propto (\Delta h)^{-\alpha}$, with $\alpha = 2$. For anisotropic cases, numerically computed distributions confirm the power-law form of the distribution with different values for the exponent α. Using the algebraic distribution from, local scaling exponents governing the scaling of spatio-temporal q^{th} order correlation functions can be derived. Also, consistency in the scaling equations implies an estimate for the global roughness exponent $\chi = 1/(\alpha - 1)$. Our results show that the single-valued interfaces of the fractal growth models exhibit intrinsic anomalous scaling [107] and multiscaling [115]. To enable simulations of large enough system sizes in the diffusion limited aggregation (DLA) model, an *exact* and efficient simulation method to speed up on-lattice random walk in complicated surroundings has been developed. The method enables convenient simulation of the DLA without any approximations with lattice sizes that have not been reachable earlier.

The subjects studied in this thesis raise questions and suggest further topics of research. First, it is evident that in order to get quantitative confirmation to the predicted corrections-to-scaling theory of Chapter 2 one needs to go up at least one to two decades in the cluster sizes. This would require for example parallelization of the Potts simulation code. Second, it would be interesting to study if modifications of the interaction in the deposition models presented in Chapter 3 affect any of the measured quantities. Further work in this direction is currently being done with a model in which the strength of the *attractive* interaction depends on the mutual overlap area of the deposited particles. Third, the earlier work by Castro *et al.* [72] suggests that adding a tunable drift and noise reduction to the DLA model would enable one to study a crossover from unstable growth to KPZ type of growth. Finally, it is not obvious how $P(\Delta h)$ is determined in higher dimensional cases. Preliminary data on 3D invasion percolation model suggests that the 2D theory for the distribution exponent α does not hold. It would be of great interest to gain understanding in these topics.

Appendix A: Measurement of the Cluster Subsets

The total mass of the cluster is defined as the number of occupied bonds in the cluster.

To determine the singly connected bonds and bonds belonging to the hull, we first identified the upper right and the lower left corners of the cluster, which we chose to serve as terminals A and B. As usual, the singly connected bonds are those that cannot be removed without destroying the connectivity between the terminals. We identified the singly connected bonds by performing two biased walks from A to B [8]. First walker chooses always the left-most possible route, thus following the left hand edge of the cluster until it reaches B. The second walker prefers turning right, and it maps the right hand edge of the cluster. The singly connected bonds are those bonds that both walkers have visited. Additionally, the hull is given by the bonds, which are visited by either walker.

The external perimeter (EP) was identified by a biased walk starting from the left vacant neighbor of terminal A. The walker goes around the external surface of the cluster on nearest-neighbor vacant sites. From the sites the walker visits, all bonds touching the cluster are counted.

In addition, we measured the number of narrow gate fjords, which is of interest because of the recently obtained exact result by Aizenman *et al.* [19]. Fjords of different gate sizes (S_G) were measured during the walk on the EP. The walker starts from the left vacant neighbor of terminal A and goes around the cluster on the EP always trying to turn to the right. At each site, we look at the neighbors on the left hand side and check whether the sites within a predefined distance S_G belong to EP or not. If the sites (and bonds) up to a distance S_G are not EP sites and the site at the distance S_G belongs to EP, the walker is about to enter a fjord with a gate size S_G. If the walker was in a fjord of a gate size S_G, fjords with gate size $S'_G > S_G$ were not allowed in

the statistics. In practise, all measured values of S_G gave similar results so that we only discuss the $S_G = 1$ case here.

As noted by Aizenman *et al.* [19], the scaling concerns fjords that are comparable in size to the cluster, and the width of the gate of which is very small comparable to the fjord size (L_F). The reason for this is easy to understand since small kinks and pits are a natural part of the fractal cluster's perimeter. Thus, only large enough fjords were included in the statistics. This was taken into account by a suitably chosen parameter s so that only fjords whose linear size was larger than the fraction sR, $L_F > sR$, where R is the cluster size, were counted.

Appendix B: Invasion Percolation Simulations

We study the IP model with periodic boundary conditions in the lateral direction. The numerical simulations of the IP lattice models were done on a 2D rectangular lattices of lateral sizes L, with $L = 32 - 4096$. The bottom row is initially occupied by the invading fluid. At each time step, one searches for the nearest neighbor (NN) perimeter sites that are occupied by the defending fluid, chooses the one with the smallest capillary number and occupies it by the invading fluid. This process is then repeated until the invasion cluster reaches the top of the lattice.

The main algorithmic aspect in our simulations is that the list of active growth sites is implemented via a balanced binary search tree (see e.g. Refs. [123, 124, 125]). By this method, the insertion and deletion operations on the list can be performed in time $\propto \ln(n)$, where n is the list size. In the case of TIP, one has to at each time step check if an the newly invaded site caused a region of defending fluid to be trapped.

For this purpose we devised the following method: All local configurations consisting of the newly invaded site and its eight neighbors are enumerated. The configurations that cause trapping are labelled, and at each time step one can by computing the configuration number decide whether trapping occured.

If the configuration is found to cause trapping of the defending fluid within a region surrounded by the invading fluid, the active perimeter sites within the trapped region are removed from the list of growth sites. This is done by starting oriented walks on the perimeter of the invading fluid [126].

Appendix C: Propagators

Since the empty space between the growing aggregate leaves is large (see Fig. (4.2), we use the following simple idea to speed up the diffusion process: Instead of taking a step of constant length (of one lattice unit), the walker investigates its surroundings to find the largest empty square of size s around it. After the square size is found, we use the appropriate exact *discrete* probability distribution to project the particle on to the surface of the empty square. This way, particle replaces $\mathcal{O}(s^2)$ steps of ordinary random walk by a single leap.

Consider a diffusing particle at the center of an empty square of size $s = 2\ell+1$ The exact *discrete* probability distribution P_{SQP} is used to project the particle to the boundary of the square (the subscript SQP refers to square propagator, since the method propagates the particle through a random route from the center to the boundary of the square). The probability distribution for the sites k on the boundary of the square is given by

$$P_{\mathrm{SQP}}(k) = \sum_{n=1}^{s} x_n^k f(\lambda_n) x_n^{\ell+1}, \tag{1}$$

where $f(\lambda) = (\lambda_+^{\ell+1} + \lambda_-^{\ell+1})^{-1}$, $\lambda_\pm = \frac{\lambda}{2} \pm \sqrt{(\frac{\lambda}{2})^2 - 1}$, $x_n^k = \sqrt{\frac{2}{s+1}} \sin(\frac{\pi n k}{s+1})$, and $\lambda_k = 4 - 2\cos\frac{\pi k}{s+1}$, with $k = 1, 2, ..., s$. The details of the derivation of the square propagator can be found in Publication VI.

Also, to avoid time-consuming walk in the region above the highest site $\max_x h(x)$ occupied by the cluster, we define the deposition line y_{HPP} to be one lattice unit higher than $\max_x h(x)$. A new particle is always released at y_{HPP}. If the particle steps beyond y_{HPP} in the $+y$ direction, it is projected back with the appropriate probability distribution P_{HPP}, previously calculated in Ref. [127]. Here, the subscript HPP refers to the half-plane propagator, since use of P_{HPP} replaces the random walk in the half-plane

$y > y_{\mathrm{HPP}}$ by a single leap. The Fourier transform of the half-plane propagator is given by

$$\hat{P}_{\mathrm{HPP}}(q) = 2 - \cos q - \sqrt{(2 - \cos q)^2 - 1}, \tag{2}$$

from which the real space distribution is easily computed using inverse FFT.

In Publication VI, we compared different implementations of the square-propagator method. In particular, we concentrated on the index search methods, since the crucial part of the implementation is how to most efficiently find the empty space around the diffusing particle.

The so called array index search method (AI) and the multigrid index search method (MG) were shown to scale almost identically in the regime where the measurements were made.

In the AI method one stores the jump indices indicating the largest SQP that can be used in the lattice. This way one only needs to pick the index from the lattice at each step. However, after the diffusing particle sticks to the aggregate updating of the index configuration needs to be done. In the MG method one coarse grains the lattice hierarchically in such a way that at each level a block of 2×2 sites is mapped into one site at the next level. If any of the four sites in the block is occupied the site at the next level is marked occupied, else it is marked empty. This way one needs $\mathcal{O}(L)$ operations at most to find the largest empty square around the walker.

The prefactor of the AI method is smaller yielding better performance. However, with the MG method one can save memory by using a bit-packing procedure so that larger system sizes can be reached than with the AI method.

We also examined the efficiency of the SQP method in simulation of anisotropic step-growth model introduced by Heinonen *et. al.* [127]. For that model, most convenient and also very efficient way to find the largest possible steps the walker can take was to use simple linear search (see Publication VI for details). Also here a factor of L is won in scaling of CPU time per particle with the system size.

Bibliography

[1] J. Asikainen, A. Aharony, B. B. Mandelbrot, E. Rausch, and J. P. Hovi (unpublished).

[2] E. Ising, Z. Phys. **21**, 613 (1925).

[3] R. B. Potts, Proc. Camb. Phil. Soc **48**, 106 (1952).

[4] S. R. Broadbent and J. M. Hammersley, Proc. Camb. Phil. Soc. **53**, 629 (1957).

[5] T. A. Witten and L. M. Sander, Phys. Rev. Lett. **47**, 1400 (1981).

[6] B. B. Mandelbrot, *Fractal Geometry of Nature* (Freeman, San Francisco, 1983).

[7] F. Y. Wu, Rev. Mod. Phys. **54**, 235 (1982).

[8] D. Stauffer and A. Aharony, *Introduction to Percolation Theory*, revised 2nd edition ed. (Taylor and Francis, Burgess Science Press, Basingstoke, London, 1994).

[9] A.-L. Barabási and H. E. Stanley, *Fractal Concepts in Surface Growth* (Cambridge University Press, Great Britain, Cambridge, 1995).

[10] J. Bear, *Dynamics of Fluids in Porous Media* (Dover, New York, 1972).

[11] M. Sahimi, Rev. Mod. Phys. **65**, 1393 (1993).

[12] T. T. J. Devaney H. Ahamer and H. A. Tritthart, Fractals **9**, 61 (2001).

[13] F. Lefebvre, H. Benali, R. Gilles, E. Kahn, and R. Di Paola, Med. Phys. **22**, 381 (1995).

[14] A. Grierer, Prog. Biophys. Molec. Biol. **37**, 1 (1981).

[15] B. B. Mandelbrot, *The fractal geometry of nature* (W. H. Freedman and Company, New York, 1977).

[16] A. B. Harris, T. C. Lubensky, W. K. Holcomb, , and C. Dasgupta, Phys. Rev. Lett. **35**, 327 (1975).

[17] P. J. Reynolds, H. E. Stanley, and W. Klein, Phys. Rev. B **21**, 1223 (1980).

[18] H. Saleur and B. Duplantier, Phys. Rev. Lett. **58**, 2325 (1987)).

[19] M. Aizenman, B. Duplantier, and A. Aharony, Phys. Rev. Lett. **83**, 1359 (1999).

[20] B. Duplantier, Phys. Rev. Lett. **84**, 1363 (2000).

[21] *A Guide to Monte Carlo Simulations in Statistical Physics* (Cambridge University Press, Great Britain, Cambridge, 2000).

[22] R. Swendsen and J. Wang, Phys. Rev. Lett. **58**, 86 (1987).

[23] U. Wolf, Phys. Rev. B **228**, 379 (1989).

[24] J. G. Dash, Phys. Rep. C **38**, 177 (1978).

[25] M. A. Rubio, C. A. Edwards, A. Dougherty, and J. P. Gollub, Phys. Rev. Lett. **63**, 1685 (1989).

[26] V. K. Horváth, F. Family, and T. Vicsek, J. Phys. A **24**, L25 (1991).

[27] T. Vicsek, M. Cserzö, and V. K. Horváth, Physica A **167**, 315 (1990).

[28] J. H. Jeffries, J.-K. Zuo, and M. M. Craig, Phys. Rev. Lett. **76**, 4931 (1996).

[29] J. M. López and J. Schmittbuhl, Phys. Rev. E **57**, 6405 (1998).

[30] J. Feder, *Fractals* (Plenum Press, New York, 1988).

[31] J. W. Evans, Rev. Mod. Phys. **65**, 1281 (1993).

[32] G. Y. Onoda and E. G. Liniger, Phys. Rev. A **33**, 715 (1986).

[33] M. Deng and C. T. J. Dodson, *Paper: An Engineered Stochastic Structure* (Tappi Press, Technology Park/Atlanta,U.S.A, 1994).

[34] K. J. Niskanen and M. J. Alava, Phys. Rev. Lett. **73**, 3475 (1994).

[35] P. Nielaba and V. Privman, Phys. Rev. E **51**, 2022 (1995).

[36] N. Provatas, M. Haataja, E. Seppälä, S. Majaniemi, J. Åström, M. J. Alava, and T. Ala-Nissila, J. Stat. Phys. **87**, 385 (1997).

[37] N. Provatas, M. Haataja, J. Asikainen, S. Majaniemi, M. J. Alava, and T. Ala-Nissila, Colloids and Surfaces A **165**, 209 (2000).

[38] N. Ryde, H. Kihira, and E. Matijevic, J. Colloid Interface Sci. **151**, 421 (1992).

[39] C. A. Murray and D. G. Grier, American Scientist **83**, 238 (1995).

[40] S. Schwarzer, Phys. Rev. E **52**, 6461 (1995).

[41] G. E. Pike and C. H. Seager, Phys. Rev. B **10**, 1421 (1974).

[42] I. Balberg, Phys. Rev. B **28**, 3799 (1983).

[43] I. Balberg, C. H. Anderson, S. Alexander, and N. Wagner, Phys. Rev. B **30**, 3933 (1984).

[44] C. Vanneste, A. Gilabert, and D. Sornette, Phys. Lett. A **155**, 174 (1991).

[45] S. Feng, B. I. Halperin, and P. Sen, Phys. Rev. B **35**, 197 (1987).

[46] B. J. Last and D. J. Thoules, Phys. Rev. Lett. **27**, 1719 (1971).

[47] I. Balberg, Phil. Mag. B **56**, 991 (1987).

[48] N. Provatas, M. J. Alava, and T. Ala-Nissila, Phys. Rev. E **54**, R36 (1996).

[49] A. Koponen, D. Kandhai, E. Hellén, M. J. Alava, A. Hoekstra, M. Kataja, K. Niskanen, P. Sloot, and J. Timonen, Phys. Rev. Lett. **80**, 716 (1998).

[50] P. Meakin, in *Phase Transitions and Critical Phenomena*, edited by C. Domb and J. L. Lebowitz (Academic, London, 1988), Vol. 12, p. 335.

[51] A. Bunde and S. Havlin, *Fractals and Disordered Systems* (Springer, Berlin, 1991).

[52] M. Dubé, M. Rost, K. R. Elder, M. J. Alava, S. Majaniemi, and T. Ala-Nissila, Phys. Rev. Lett. **83**, 1628 (1999); European Phys. J. B **15**, 701 (2000).

[53] J. Krug, Advances in Physics **46**, 139 (1997).

[54] M. Kardar, G. Parisi, and Y.-C. Zhang, Phys. Rev. Lett. **79**, 889 (1986).

[55] E. Medina, T. Hwa, M. Kardar, and Y.-C. Zhang, Phys. Rev. A **39**, 3053 (1989).

[56] H. K. Janssen, U. C. Täuber, and E. Frey, Eur. Phys. J. B **9**, 491 (1998).

[57] S. Buldyrev, S. Havlin, J. Kertész, H. E. Stanley, and T. Vicsek, Phys. Rev. A **43**, 7113 (1991).

[58] Y.-C. Zhang, J. Phys. (Paris) **51**, 2113 (1990).

[59] Y.-C. Zhang, Physica A **170**, 1 (1990).

[60] J. Krug, J. Phys. I (France) **1**, 9 (1990).

[61] L. Chi-Hang and L. M. Sander, Phys. Rev. Lett. **69**, 3338 (1992).

[62] L. Chi-Hang and L. M. Sander, Phys. Rev. E **48**, 979 (1993).

[63] P. Meakin, P. Ramanlal, L. M. Sander, and R. C. Ball, Phys. Rev. A **34**, 5091 (1986).

[64] F. Family and T. Viscek, J. Phys. A **18**, L75 (1985).

[65] T. Salditt and H. Spohn, Phys. Rev. E **47**, 3524 (1993); J. Heinonen, I. Bukharev, T. Ala-Nissila, and J. M. Kosterlitz, Phys. Rev. E **57**, 6851 (1998); M. Dubé, M. Rost, K. R. Elder, M. J. Alava, S. Majaniemi, and T. Ala-Nissila, Phys. Rev. Lett. **83**, 1628 (1999); European Phys. J. B **15**, 701 (2000).

[66] J. Heinonen, I. Bukharev, T. Ala-Nissila, and M. Kosterlitz, Phys. Rev. E **57**, 6851 (1998).

[67] L. H. Tang H. Leschhorn, Phys. Rev. A **45**, R8390 (1992).

[68] L. H. Tang, M. Kardar, and D. Dhar, Phys. Rev. Lett. **74**, 290 (1995).

[69] M.-P. Kuittu, M. Haataja, N. Provatas, and T. Ala-Nissila, Phys. Rev. E **58**, 1514 (1998).

[70] M.-P. Kuittu, M. Haataja, N. Provatas, and T. Ala-Nissila, Phys. Rev. E **59**, 2677 (1998).

[71] T. Vicsek, *Fractal Growth Phenomena* (World Scientific, Singapore, 1992); For a review, see *Fractals in Natural Science*, edited by T. Vicsek, M. Schlesinger, and M. Matsuhita (World Scientific, Singapore, 1993).

[72] M. Castro, R. Cuerno, A. Sánchez, and F. Domínguez-Adame, Phys. Rev. E **57**, R2491 (1998).

[73] A. Coniglio, Phys. Rev. Lett. **62**, 3054 (1989).

[74] J. L. Cardy, M. Nauenberg, and D. J. Scalapino, Phys. Rev. B **22**, 2560 (1980).

[75] M. P. M. den Nijs, Phys. Rev. B **27**, 1674 (1983).

[76] J. Hoshen, M. W. Berry, and K. S. Minser, Phys. Rev. E **56**, 1455 (1997).

[77] The total mass of the cluster is the same as the number of sites belonging to the cluster.

[78] The hull is the set of sites belonging to the cluster, that have one or more vacant nearest neighbor sites, and that can be connected to infinity by a line not crossing the cluster.

[79] The external perimeter is the set of vacant sites that have a nearest neighbor site belonging to the cluster and that can be connected to infinity by a line not crossing the cluster.

[80] Singly connected sites are such that if one removes one of them, the cluster breaks in disconnected parts.

[81] By gates to fjords, narrow (relative to the cluster's linear size)openings to large fjords (as compared to the size of the cluster) on the cluster's perimeter are meant [19].

[82] C. M. Fortuin and P. W. Kasteleyn, Physica (Utrecht) **57**, 536 (1972).

[83] S. Alexander, Phys. Lett. A **54**, 353 (1975).

[84] M. Bretz, Phys. Rev. Lett. **38**, 501 (1977).

[85] E. Domany, M. Schick, and J. S. Walker, Phys. Rev. Lett. **38**, 1148 (1977).

[86] T. Grossman and A. Aharony, J. Phys. A **19**, L745 (1986).

[87] A. Coniglio, J. Phys. A **15**, 3829 (1982).

[88] N. Metropolis, A. W. Rosenbluth, M. N. Rosenbluth, A. M. Teller, and E. Teller, J. Chem. Phys **21**, 1087 (1953).

[89] B. Nienhuis, A. N. Berker, E. K. Riedel, and M. Schick, Phys. Rev. Lett. **43**, 737 (1979).

[90] M. Nauenberg and D. J. Scalapino, Phys. Rev. Lett. **44**, 837 (1980).

[91] C. Vanderzande and J. F. Marko, J. Phys. A **26**, 7391 (1993).

[92] A. Aharony and G. Ahlers, Phys. Rev. Lett. **44**, 782 (1980).

[93] A. Aharony Y. Gefen, B. B. Mandelbrot and A. Kapitulnik, J. Stat. Phys **36**, 827 (1984).

[94] B. B. Mandelbrot, Y. Gefen, A. Aharony, and J. Peyriere, J. Phys. A **18**, 335 (1985).

[95] M. E. J. Newman and R. M. Ziff, Phys. Rev. Lett. **85**, 4104 (2000).

[96] J. Hoshen and R. Kopelman, Phys. Rev. B **14**, 3438 (1976).

[97] William H. Press, Saul A. Teukolsky, and William T. Vetterlingand Brian P. Flannery, *Numerical Recipies in C: The Art of Scientific Computing* (Cambridge University Press, Great Britain, Cambridge, 1992).

[98] M. E. Fisher, Physics **3**, 255 (1967).

[99] N. Goldenfeld, *Lectures on phase transitions and the renormalization group* (Addison - Wesley Publishing Company, USA, 1992).

[100] J. Åström, Master's thesis, Åbo Akademi, 1989.

[101] N. Provatas, T. Ala-Nissila, and M. J. Alava, Phys. Rev. Lett. **75**, 3556 (1995).

[102] J. Asikainen and T. Ala-Nissila, Phys. Rev. E **61**, 5002 (2000).

[103] S. B. Lee and S. Torquato, Phys. Rev. A **41**, 5338 (1990).

[104] R. M. Ziff and R. D. Vigil, J. Phys. A: Math. Gen. **23**, 5103 (1990).

[105] B. Ghosh, Calcutta Math. Soc. **43**, 17 (1951).

[106] R. P. U. Karunasiri, R. Bruinsma, and J. Rudnick, Phys. Rev. Lett. **62**, 788 (1989); G. S. Bales and A. Zangwill, Phys. Rev. Lett. **63**, 692 (1989).

[107] J. J. Ramasco, J. M. López, and M. A. Rodríguez, Phys. Rev. Lett. **84**, 2199 (2000).

[108] J. Krug, Phys. Rev. Lett. **72**, 2907 (1994).

[109] S. Das Sarma, Phys. Rev. E **53**, 1996 (1996).

[110] J. M. López and M. A. Rodríguez, Phys. Rev. E **54**, R2189 (1996).

[111] G.-C. Wang H.-N. Yang and T.-M. Lu, Phys. Rev. Lett. **73**, 2348 (1994).

[112] A. Sánchez and M. J. Bernal, J. Non-Cryst. Solids **160**, 18 (1993).

[113] J. M. López, M. A. Rodríquez, and R. Cuerno, Phys. Rev. E **56**, 3993 (1997).

[114] M. Myllys, J. Maunuksela, M. J. Alava, T. Ala-Nissila, J. Merikoski, and J. Timonen, Phys. Rev. E **64**, 036101 (2001).

[115] A.-L. Barabási, R. Bourbonnais, M. Jensen, J. Kertész, T. Vicsek, and Y.-C. Zhang, Phys. Rev. A **45**, R6951 (1992).

[116] M. Paczuski, S. Maslov, and P. Bak, Phys. Rev. E **53**, 414 (1996).

[117] J. M. López, Phys. Rev. Lett. **83**, 4594 (1999).

[118] D. J. Wilkinson and J. Willemsen, J. Phys. A **16**, 3365 (1983).

[119] M. Dias and D. Wilkinson, J. Phys. A **19**, 3131 (1986).

[120] R. A. Roy and R. Messier, Mat. Res. Soc. Symp. Proc. **38**, 363 (1985); R. Messier and J. E. Yehoda, J. Appl. Phys. **58**, 3739 (1985); R. Messier, J. Vac. Sci. Technol. A **4**, 490 (1986); T. Salditt *et al.*, Europhys. Lett. **36**, 565 (1996).

[121] To enable simulations of the ballistic deposition model in large enough systems, we use bit-packing procedure for the BD model. Each 32 bit integer of the simulation lattice describes the state of 32 sites of the "macro-lattice". In practice, we pack the lattice in the direction perpendicular to the substrate. Thus the periodic boundaries in the parallel direction are easily implemented. The largest system size used in the BD simulations was $L = 131072$.

[122] J. Yu and J. G. Amar, Phys. Rev. E **66**, 021603 (2002).

[123] A. P. Sheppard, M. A. Knackstedt, W. V. Pinczewski, and M. Sahimi, J. Phys. A **32**, L521 (1999).

[124] M. A. Knackstedt, M. Sahimi, and A. Sheppard, Phys. Rev. E **61**, 4920 (2000).

[125] S. Schwarzer, A. Shlomo, and A. Bunde, Phys. Rev. E **59**, 3262 (1999).

[126] P. Meakin, Physica A **173**, 305 (1991).

[127] J. Heinonen, I. Bukharev, T. Ala-Nissila, and J. M. Kosterliz, Phys. Rev. E **57**, 6851 (1998).